Petrologie sedimentárních hornin

G421P13, ZS 2/1, 3-4.roč.

# *4. Evapority, silicity, ferolity, fosfáty*

Karel Martínek

Ústav geologie a paleontologie

# *Evapority*

chemismus mořské vody, minerální sukcese při izotermickém odpařování mořské vody

sedim. prostředí: subakvatické, subaerické - sabcha, okraj šelfu - laguna, salina, izolovaná pánev, playa

mikrostruktury sádrovec-anhydrit, halit, lakustrinní evapority

laterální a vertikální distribuce facií řízené rel. pohyby hladiny

diapirismus

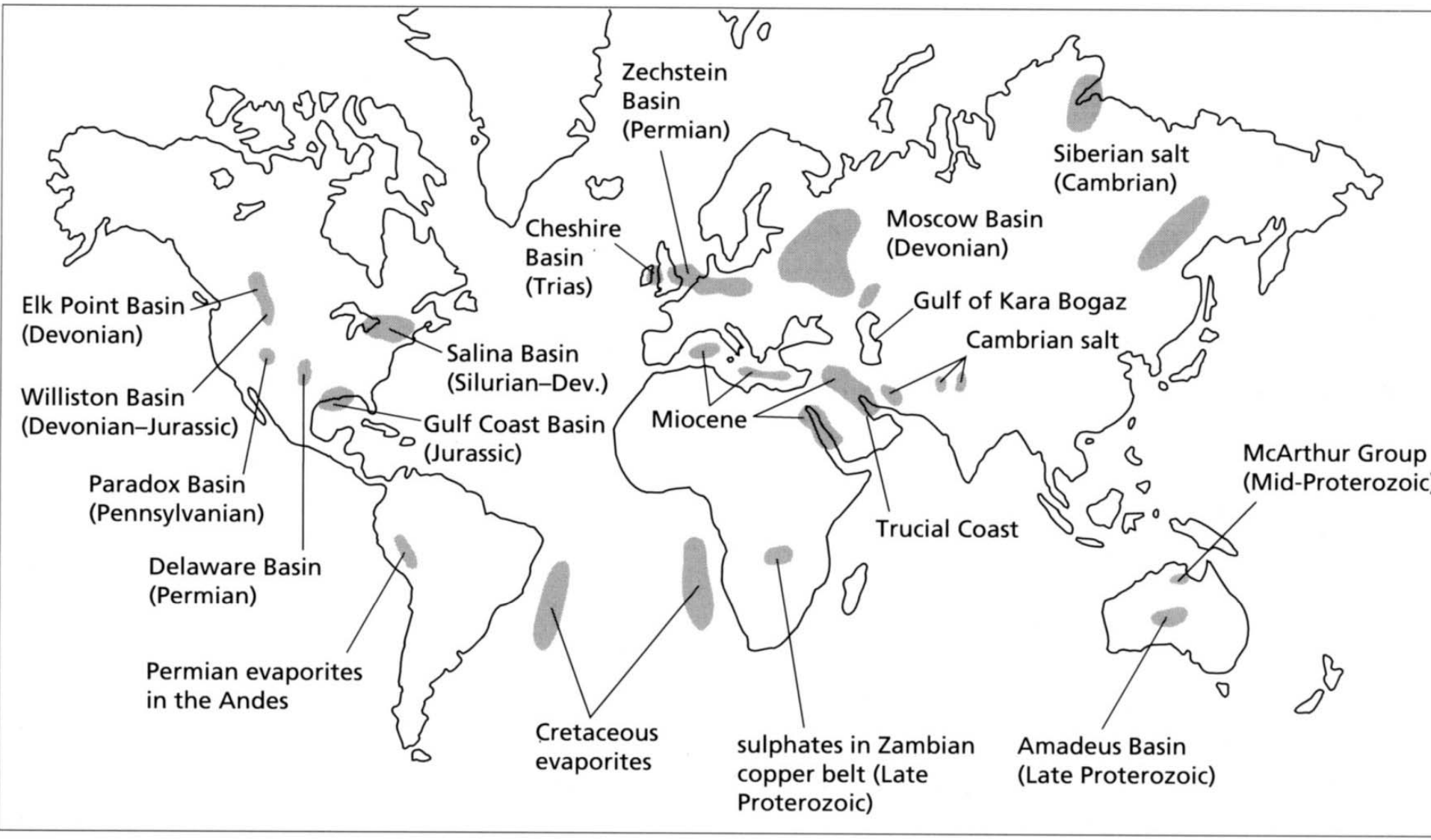
Zechstein Basin (Permian)
Siberian salt (Cambrian)
Moscow Basin (Devonian)
Cheshire Basin (Trias)
Elk Point Basin (Devonian)
Gulf of Kara Bogaz
Cambrian salt
Salina Basin (Silurian–Dev.)
Williston Basin (Devonian–Jurassic)
Gulf Coast Basin (Jurassic)
Miocene
McArthur Group (Mid-Proterozoic)
Paradox Basin (Pennsylvanian)
Trucial Coast
Delaware Basin (Permian)
Permian evaporites in the Andes
Cretaceous evaporites
sulphates in Zambian copper belt (Late Proterozoic)
Amadeus Basin (Late Proterozoic)

**Table 5.1** The common marine and non-marine evaporite minerals

| Marine evaporite minerals | | Non-marine evaporite minerals | |
|---|---|---|---|
| halite | $NaCl$ | halite, gypsum, anhydrite | |
| sylvite | $KCl$ | epsomite | $MgSO_4 . 7H_2O$ |
| carnallite | $KMgCl_3 . 6H_2O$ | trona | $Na_2CO_3 . NaHCO_3 . 2H_2O$ |
| kainite | $KMgClSO_4 . 3H_2O$ | mirabilite | $Na_2SO_4 . 10H_2O$ |
| anhydrite | $CaSO_4$ | thenardite | $NaSO_4$ |
| gypsum | $CaSO_4 . 2H_2O$ | bloedite | $Na_2SO_4 . MgSO_4 . 4H_2O$ |
| polyhalite | $K_2MgCa_2(SO_4)_4 . 2H_2O$ | gaylussite | $Na_2CO_3 . CaCO_3 . 5H_2O$ |
| kieserite | $MgSO_4 . H_2O$ | glauberite | $CaSO_4 . Na_2SO_4$ |

**Table 5.2** The composition of sea water expressed in parts per million and percentage of total dissolved species. For comparison, the composition of world average river water, with a salinity of around 120 ppm is also given. Data from Krauskopf (1979)

| | Seawater | | |
|---|---|---|---|
| Dissolved species | ppm | % of total | River water |
| $Cl^-$ | 18 000 | 55.05 | 7.8 |
| $Na^+$ | 10 770 | 30.61 | 6.3 |
| $SO_4^{2-}$ | 2715 | 7.68 | 11.2 |
| $Mg^{2+}$ | 1290 | 3.69 | 4.1 |
| $Ca^{2+}$ | 412 | 1.16 | 15.0 |
| $K^+$ | 380 | 1.10 | 2.3 |
| $HCO_3^-$ | 140 | 0.41 | 58.4 |
| $Br^-$ | 67 | 0.19 | 0.02 |
| $H_3BO_3$ | 26 | 0.07 | 0.1 |
| $Sr^{2+}$ | 8 | 0.03 | 0.09 |
| $F^-$ | 1.3 | 0.005 | 0.09 |
| $H_4SiO_4$ | 1 | 0.004 | 13.1 |

Tab. 19

Čtyři základní stádia krystalizace solí při izotermickém odpařování mořské vody

| stádium | hlavní produkt krystalizace | násobek koncentrace rozpuštěných látek | snížení objemu solanky |
|---|---|---|---|
| I. | karbonáty Ca | 1 - 3,35 | 0 - 1/5 |
| II. | sulfáty (hlavně sádrovec a anhydrit) | 3,35 - 10,96 | 1/5 - 1/10 |
| III. | chloridy Na (hlavně helit + zbytkové sulfáty) | 10,96 - 60,43 | 1/10 - 1/20 |
| IV. | chloridy a sulfáty K a Mg (+ malé množství halitu a Ca sulfátu) | nad 60,43 | nad 1/20 |

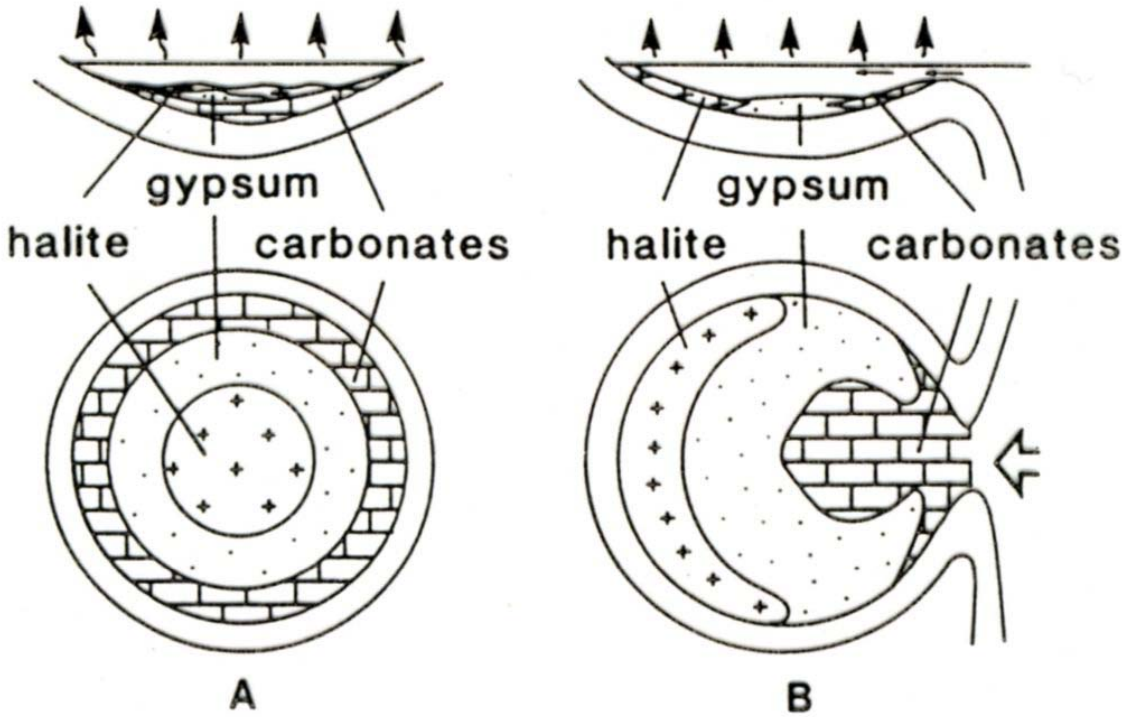


**Fig. 5.20** Broad patterns of evaporite facies. A, Bullseye pattern, with the most soluble salts in the basin centre, typical of completely enclosed basins. B, Tear-drop pattern, typical of restricted basins with near-permanent connection to the open ocean, where the most soluble salts occur farthest away form the basin entrance. After Schmaltz (1969).

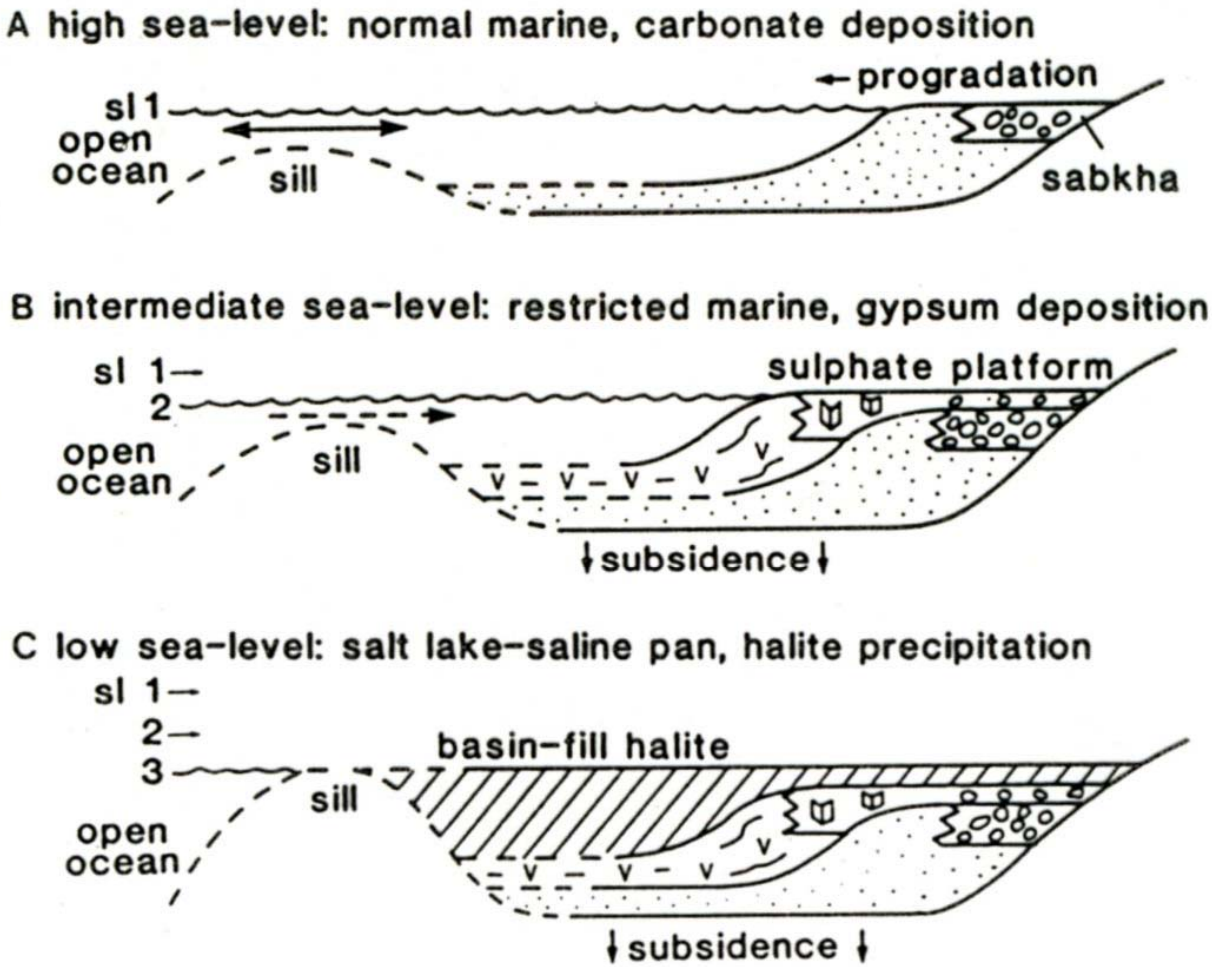


**Fig. 5.21** Model for evaporite deposition in an intracratonic basin, where eustatic sea-level changes are a major control. After Clark & Tallbacka (1980).

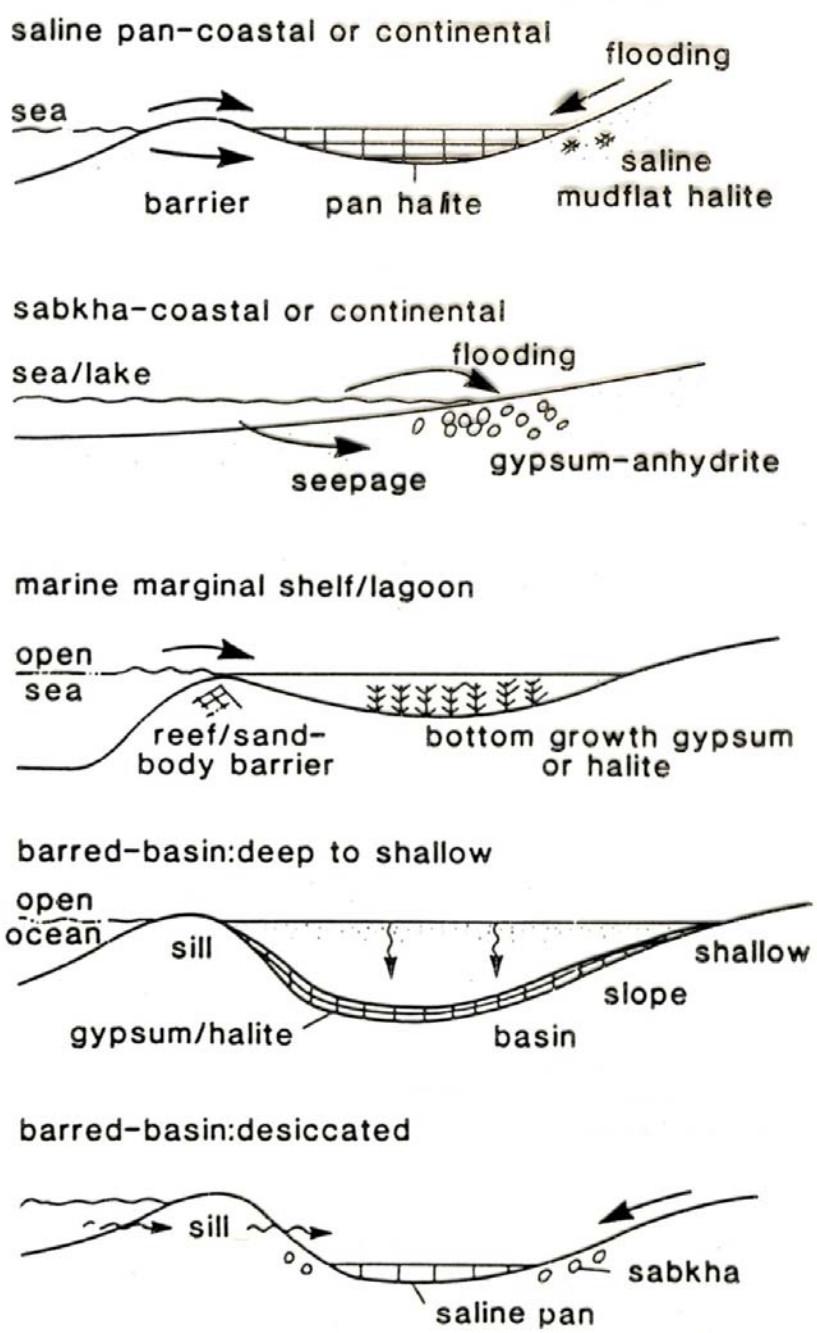


**Fig. 5.2** Principal depositional environments of evaporites.

**Table 5.3** The theoretical thickness of salts precipitated from sea water compared with the thickness of these salts in the Permian Zechstein of Germany, expressed as 100 m of precipitated evaporite. Note that there is much more $CaSO_4$ and much less Mg and K salts in the Zechstein deposits compared with the theoretical. Also shown is the approximate thickness of the various salts produced by the evaporation of a column of sea water 1000 m high. After Borchert & Muir (1964)

| Component | Mineral | Thickness in 100 m of evaporite | | Salt thickness from 1000 m of sea water |
|---|---|---|---|---|
| | | from sea water | Permian Zechstein | |
| $MgCl_2$ | in bischofite and carnallite | 9.4 | 0.5 | 1.5 |
| KCl | sylvite and in carnallite | 2.6 | 1.5 | 0.4 |
| $MgSO_4$ | in kieserite | 5.7 | 1.0 | 1.0 |
| NaCl | halite | 78 | 78 | 12.9 |
| $CaSO_4$ | anhydrite | 3.6 | 16 | 0.6 |
| $CaCO_3$ | calcite | 0.4 | 3 | 0.1 |
| $CaMg(CO_3)_2$ | dolomite | | | |

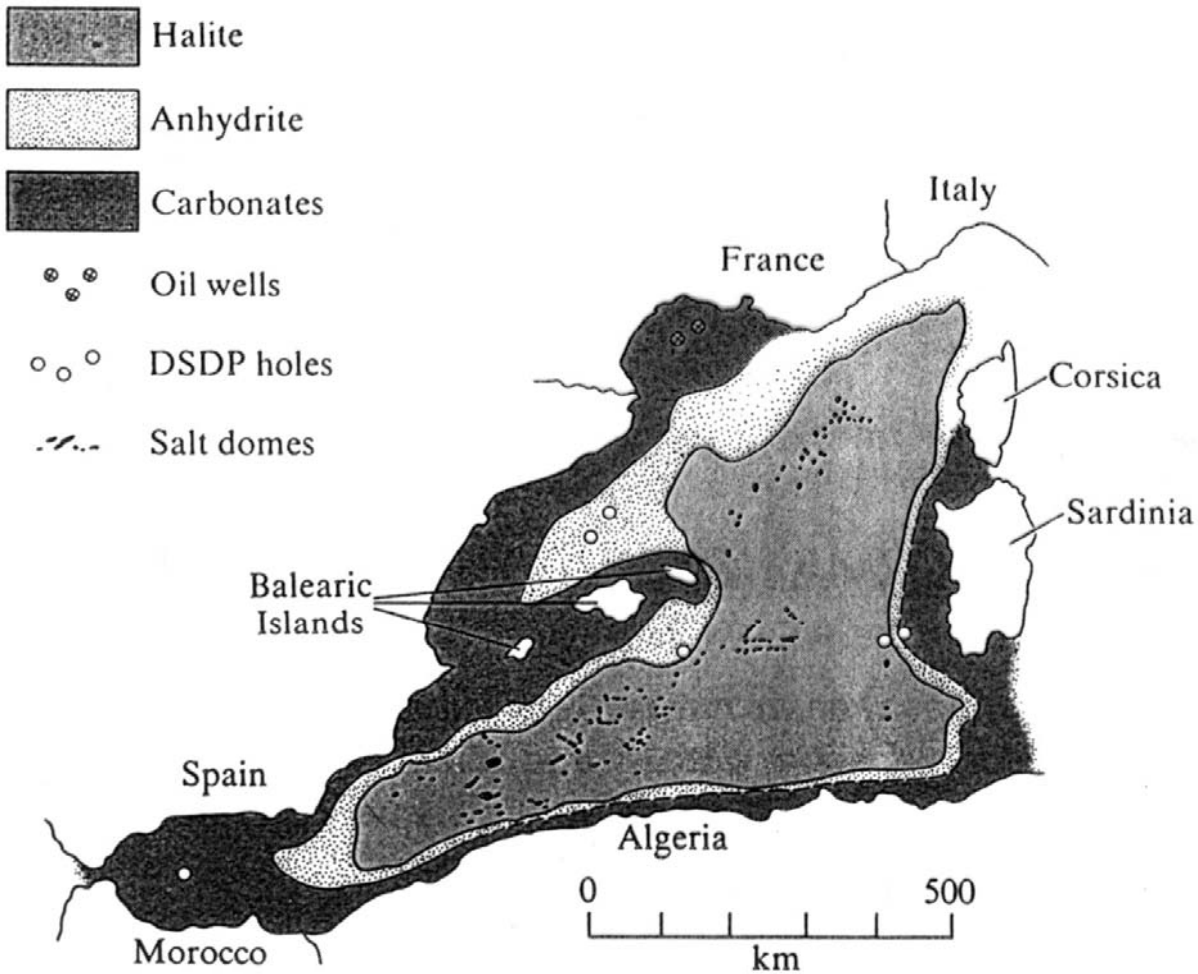


**Figure 10-21**
Evaporite distribution in Miocene rocks of Balearic Basin of Mediterranean Sea immediately east of Strait of Gibraltar. Balearic was one of several topographically low salt pans on floor of desiccated Mediterranean. Potash salts (not shown) occur in middle of halite area. [Hsü, 1972, *Earth-Science Rev., 8,* p. 390.]

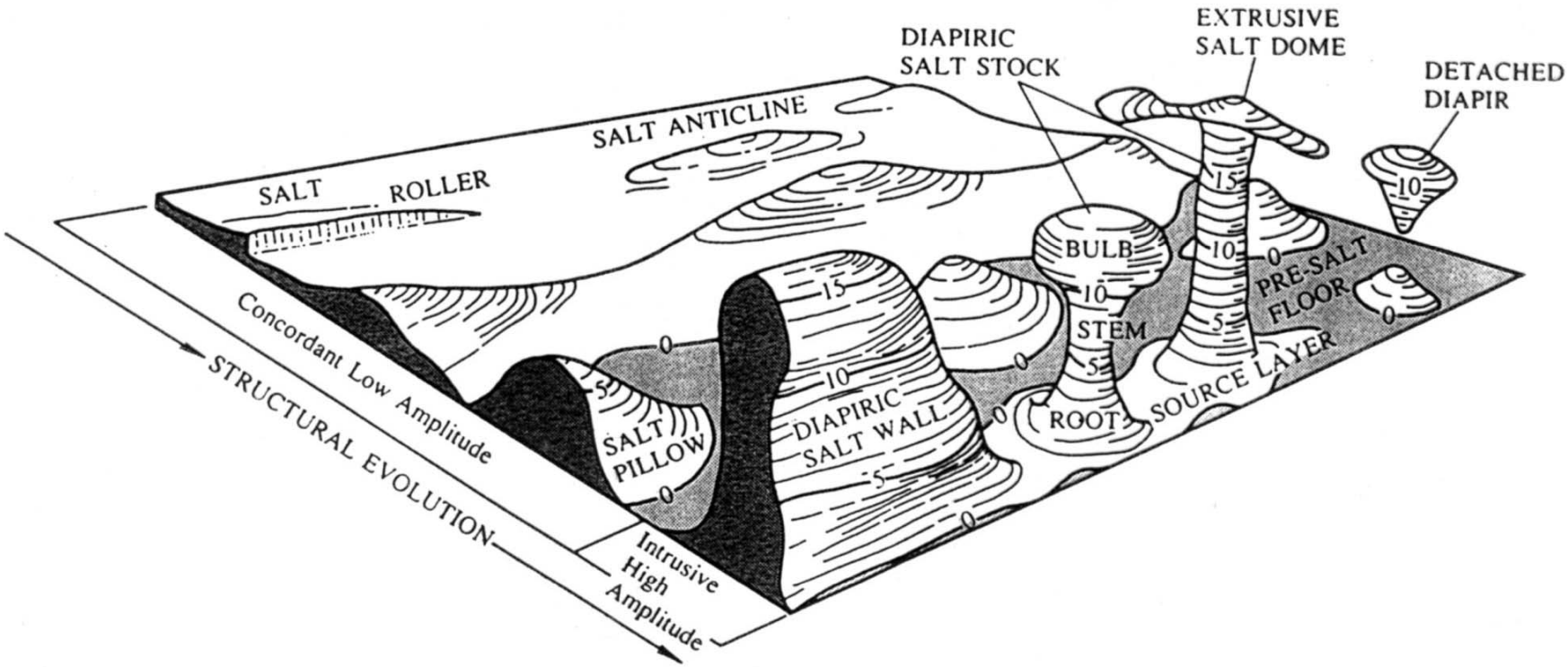


**Figure 10-11**
The main configurations of salt structures. Structure contours are in arbitrary units. Larger features such as salt nappes cannot be shown at this scale. [Jackson and Talbot, 1986, p. 306.]

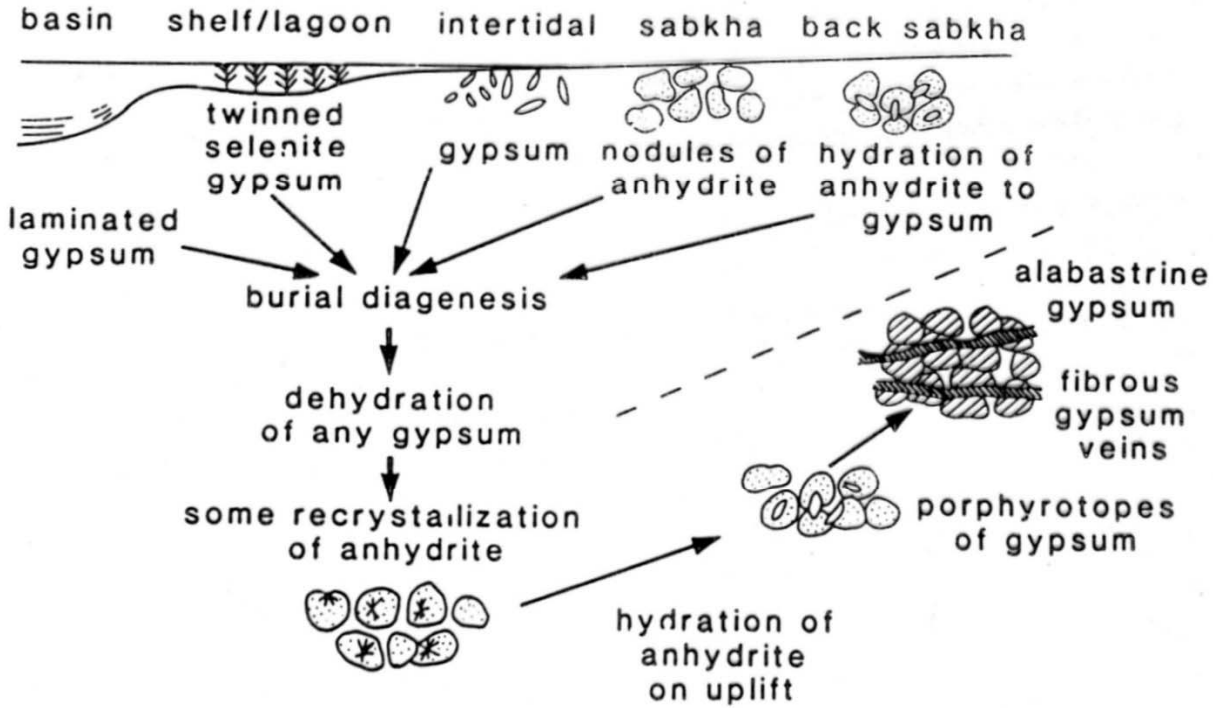


**Fig. 5.3** The 'gypsum-anhydrite cycle showing mineral and textural changes from the surface, into the subsurface and on uplift.

**Table 5.4** The water chemistry of five salt lakes (in ppm). The main point to note is the great variability in the relative concentrations of the constituents between lakes

| | Dead Sea | Great Salt Lake, Utah | Mono Lake, California | Borax Lake, California | Gulf of Kara, Bogaz, USSR |
|---|---|---|---|---|---|
| $Cl^-$ | 208 020 | 112 900 | 15 100 | 5945 | 142 500 |
| $SO_4^{2-}$ | 540 | 13 590 | 7530 | 22 | 46 900 |
| $HCO_3^-$ | 240 | 180 | 26 430 | 6668 | — |
| $Na^+$ | 34 940 | 67 500 | 21 400 | 6199 | 81 200 |
| $K^+$ | 7560 | 3380 | 1120 | 322 | |
| $Ca^{2+}$ | 15 800 | 330 | 11 | nil | 4900 |
| $Mg^{2+}$ | 41 960 | 5620 | 32 | 30.7 | 19 900 |
| Total salinity | 315 040 | 203 490 | 71 900 | >19 400 | >293 000 |

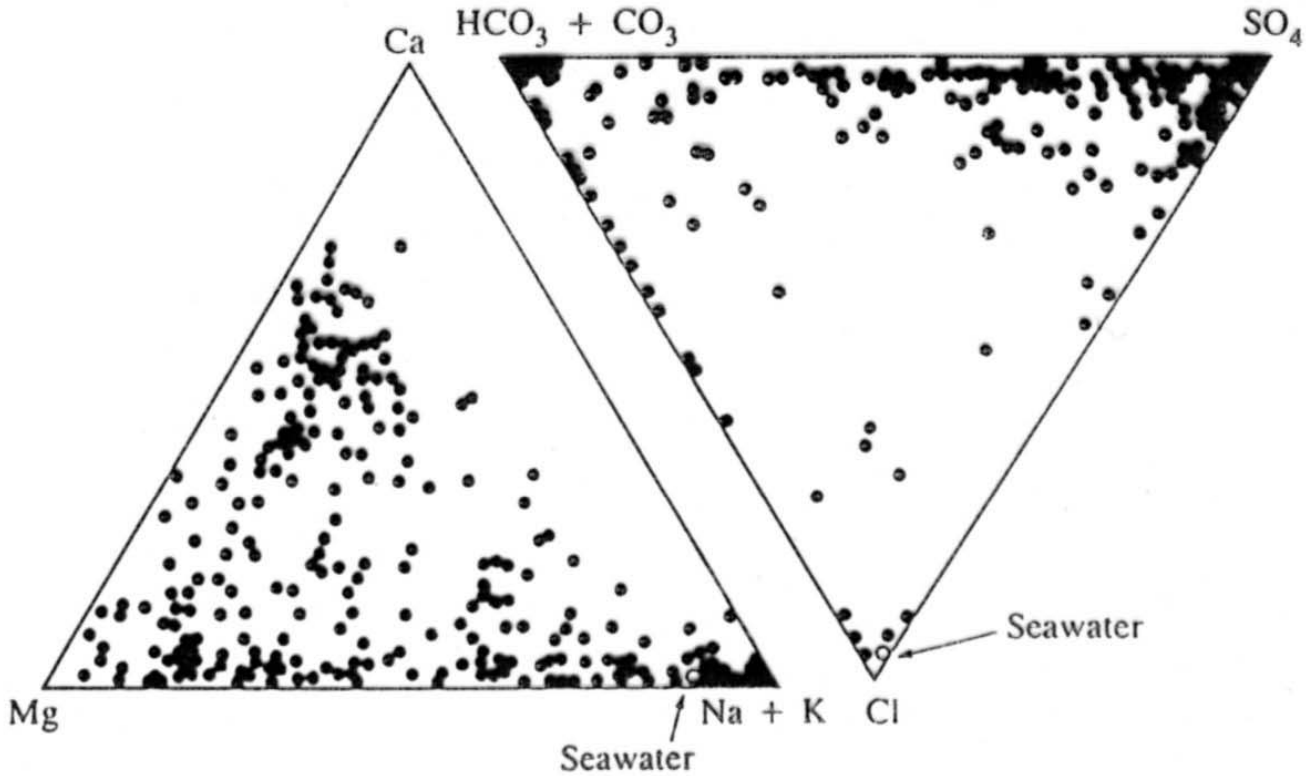


**Figure 10-3**
This triangular diagram with standard elemental poles displays water compositions for 379 saline lakes in western Canada. Also shown is the location of seawater in each triangle. It is evident that many of these waters show little or no influence of marine water. [Last, 1989, *Sedimentary Geol.*, 64, 209.]

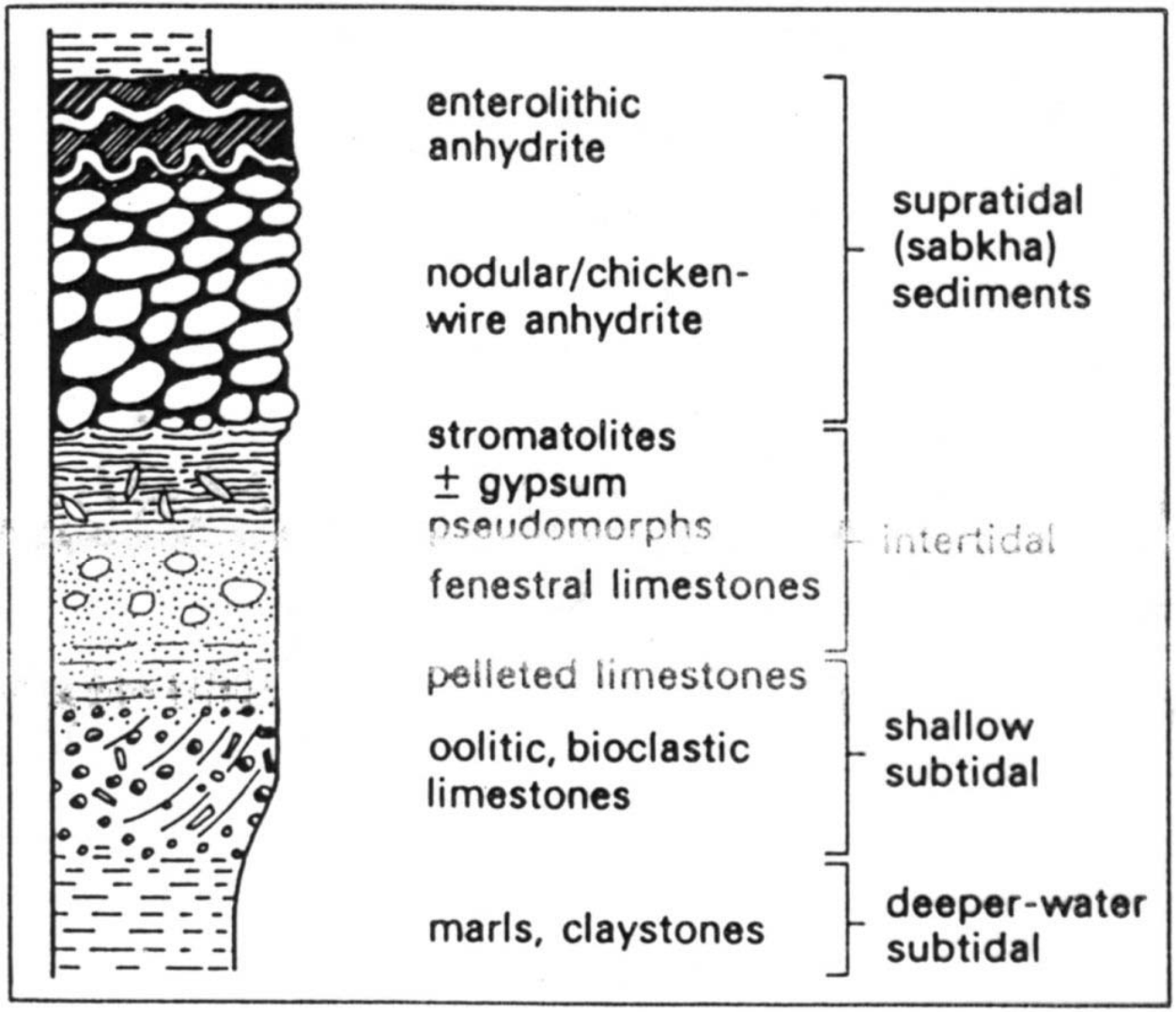


**Fig. 5.17** A sabkha cycle. Such cycles typically range from several to several tens of metres in thickness.

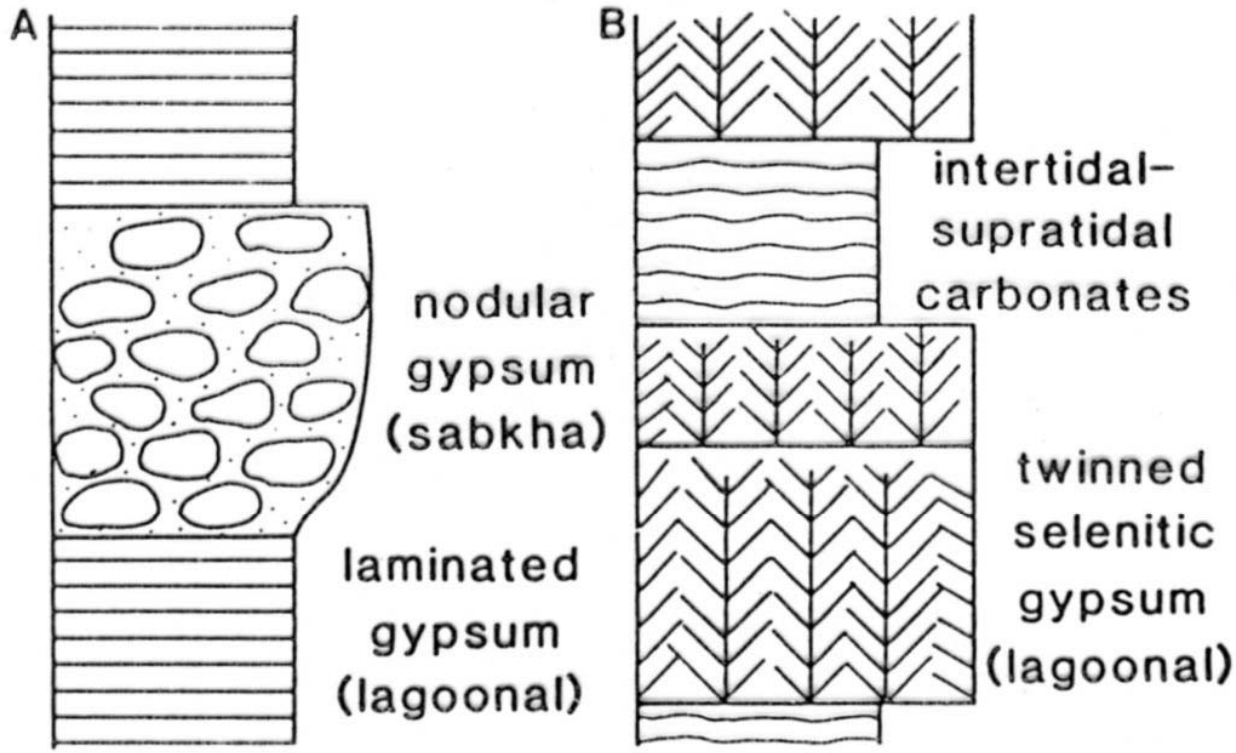


**Fig. 5.18** Two less common types of evaporite cycle. A, Laminated gypsum passing up into nodular gypsum. B, Lagoonal, selenitic gypsum passing up into intertidal–supratidal carbonates.

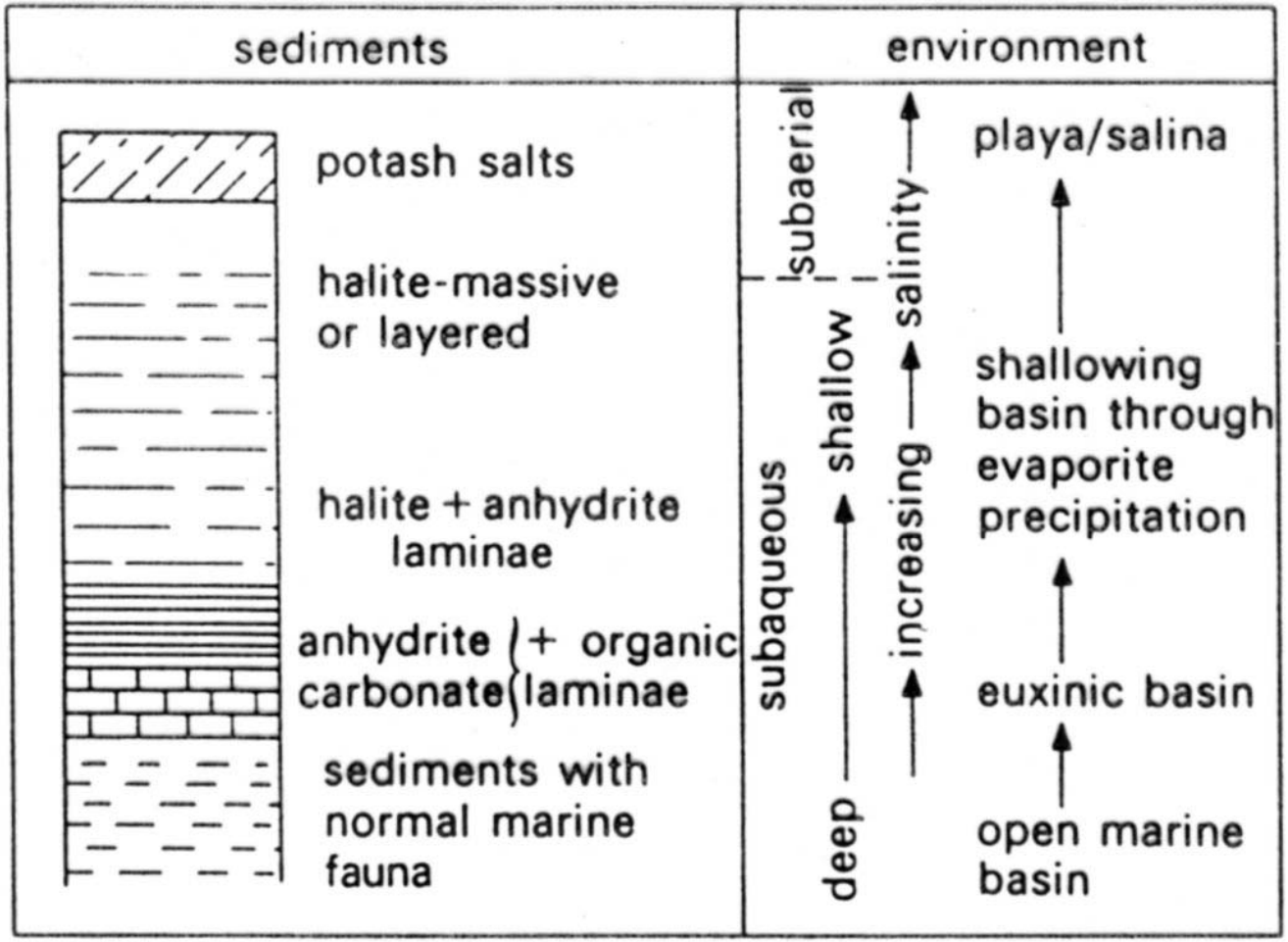


**Fig. 5.19** Evaporite sequence formed in an initially deep, marine barred-basin, with periodic replenishment.

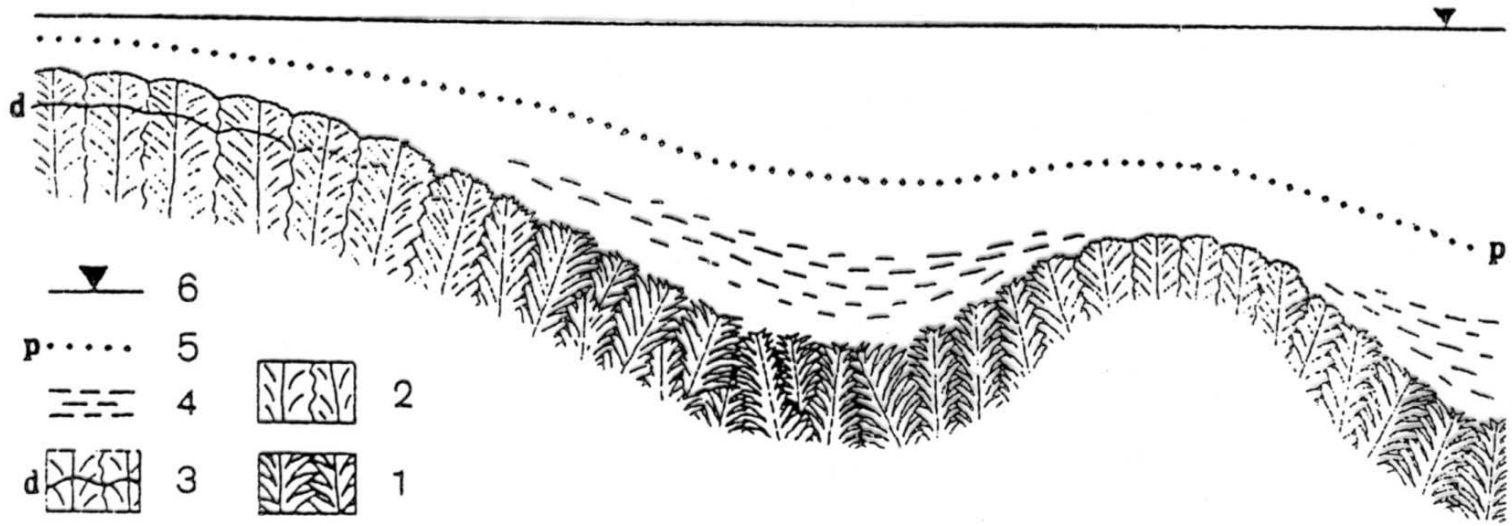


Fig. 7 *Model środowiska sedymentacji gipsów szklicowych o budowie palisadowej (subfacje 2a i 2b)*
*1 - kryształy o budowie szkieletowej (subfacja 2a), 2 - kryształy o budowie masywnej (subfacja 2b), 3 - powierzchnie rozpuszczania (d), 4 - zawiesina ilasta, 5 - pyknoklina (p), 6 - poziom wody*

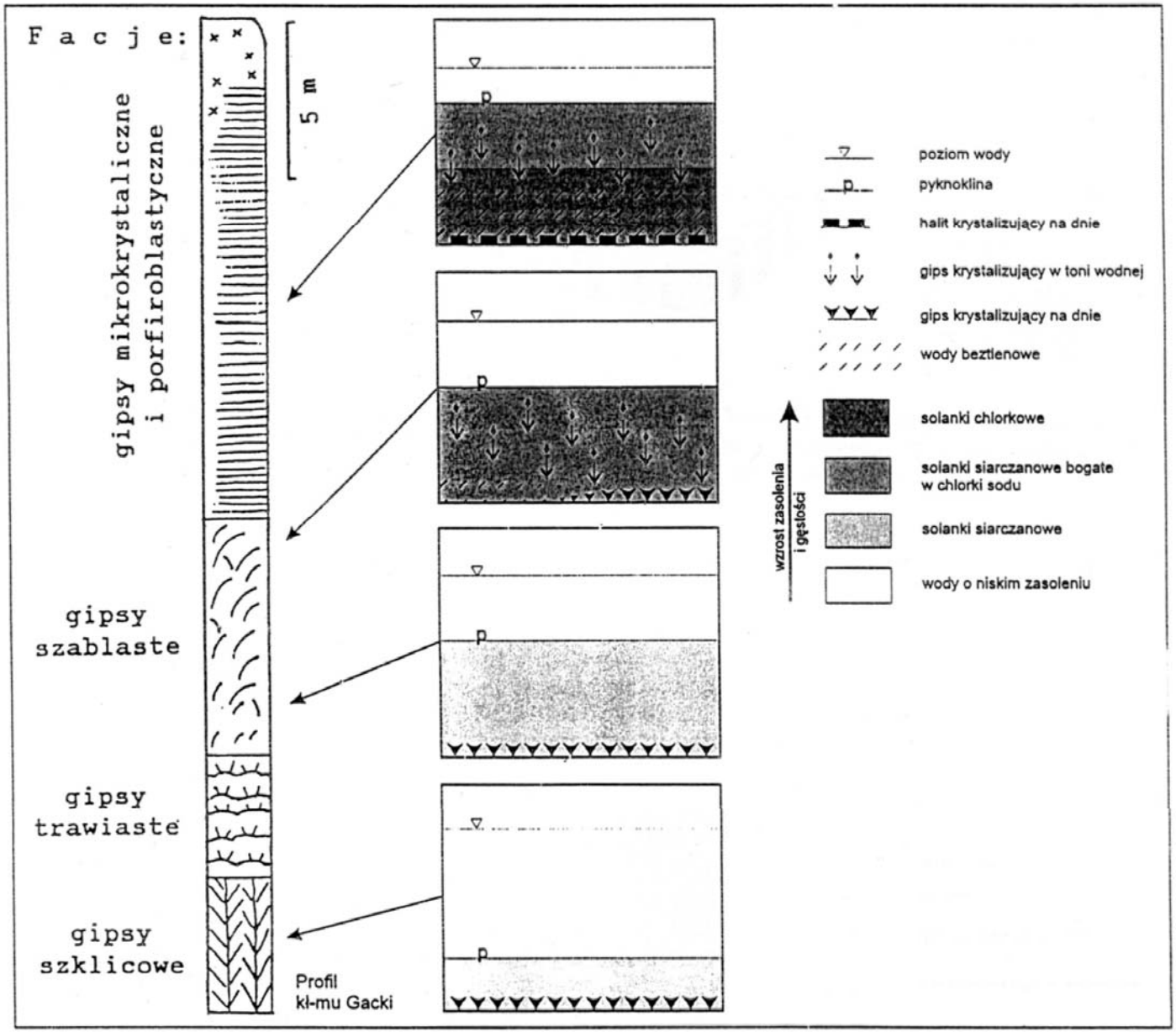


Fig. 27 *Ewolucja składu i struktury wód basenu ewaporacyjnego*

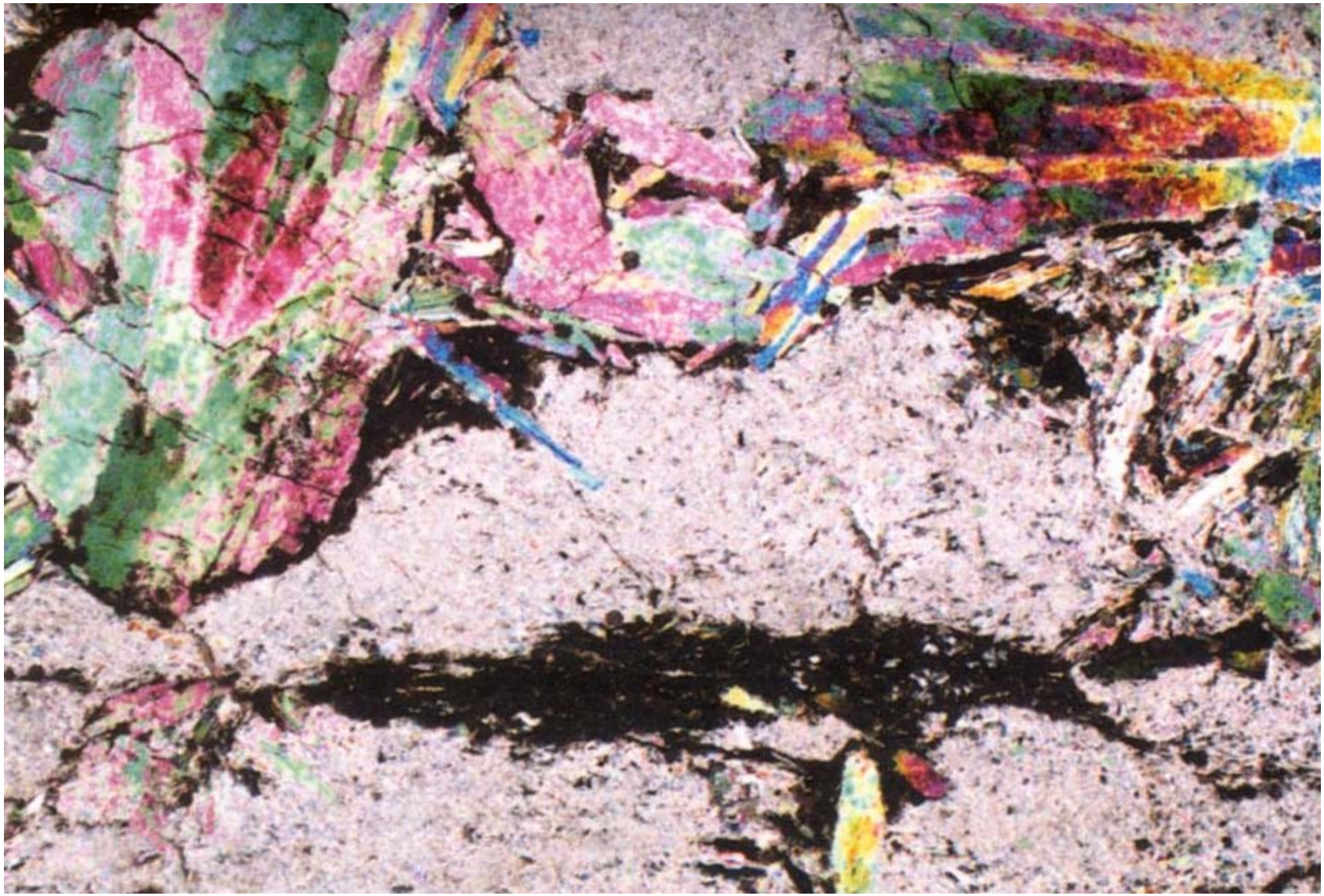

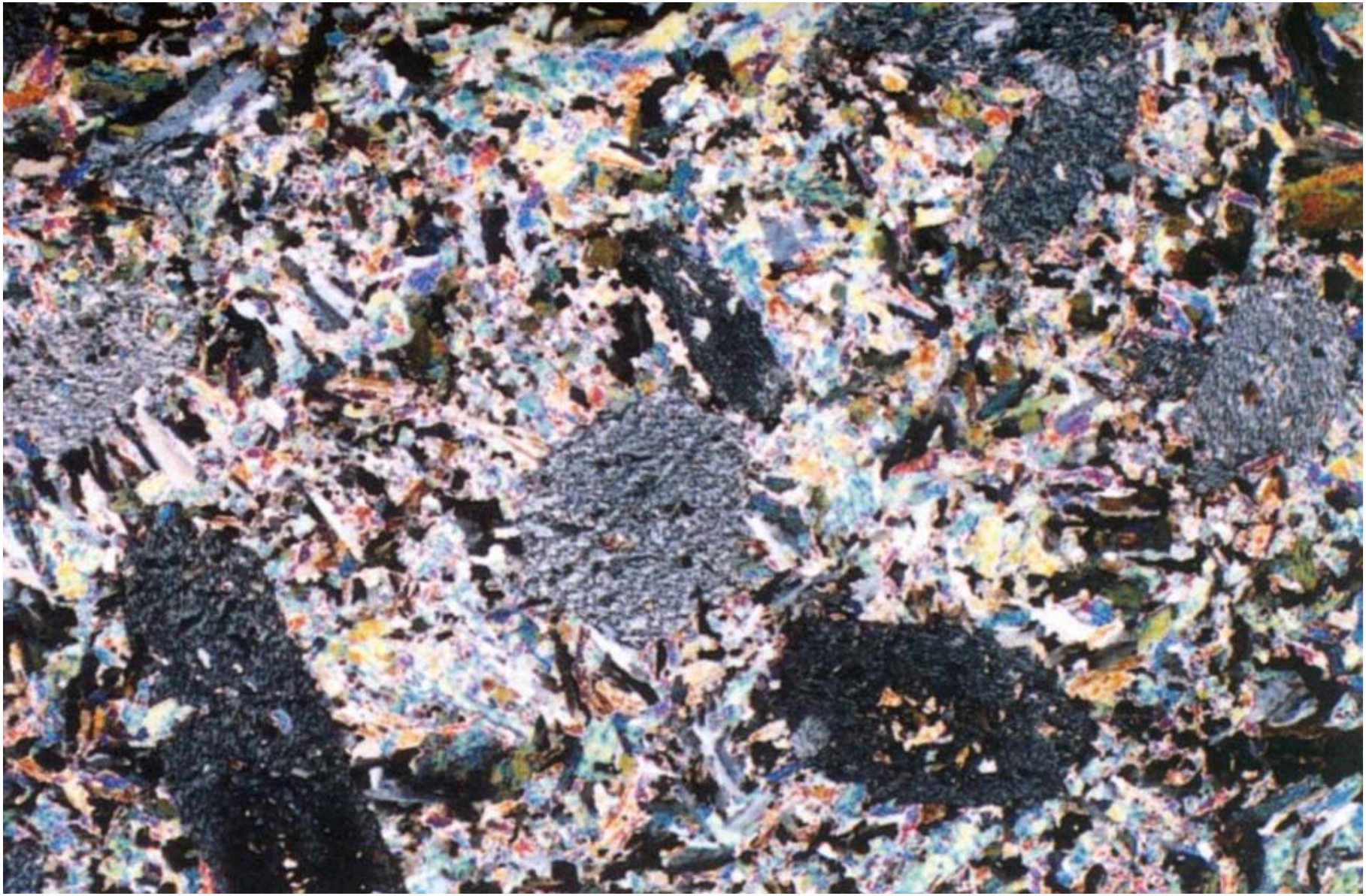

# *Silicity*

mineralogie - opál A, opál CT, křemen

mikrostruktury - euhedrální, mikrokřemen, megakřemen, chalcedonický kř.
zdroje, rozpustnost

diageneze, silicifikace mořská vs. jezerní (slaná alkalická jezera)

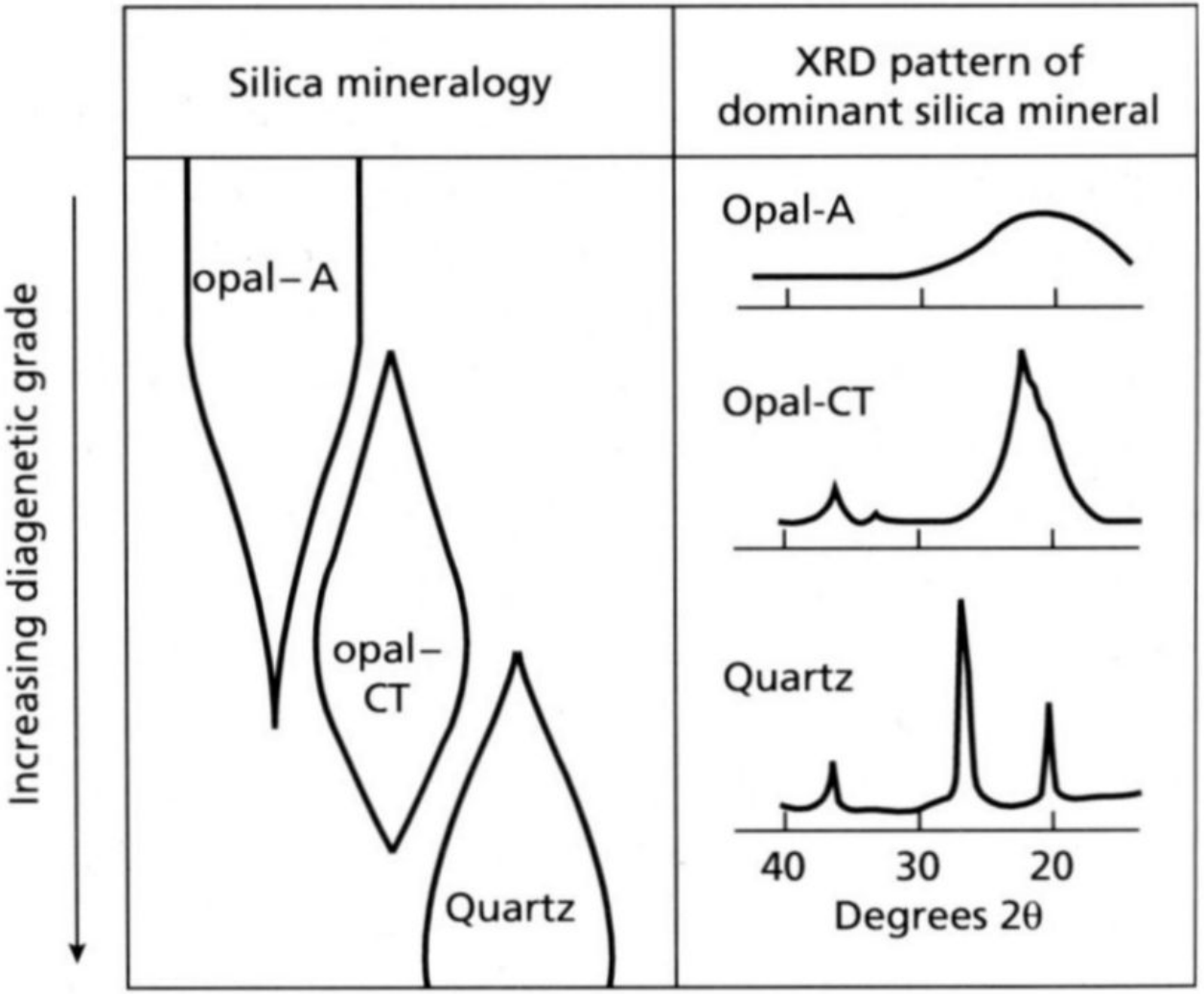


**Fig. 9.6** Schematic changes in silica mineralogy with increasing diagenesis, and X-ray diffraction patterns for opal-A, opal-CT and quartz showing the increasing crystallinity. After Pisciotto (1981).

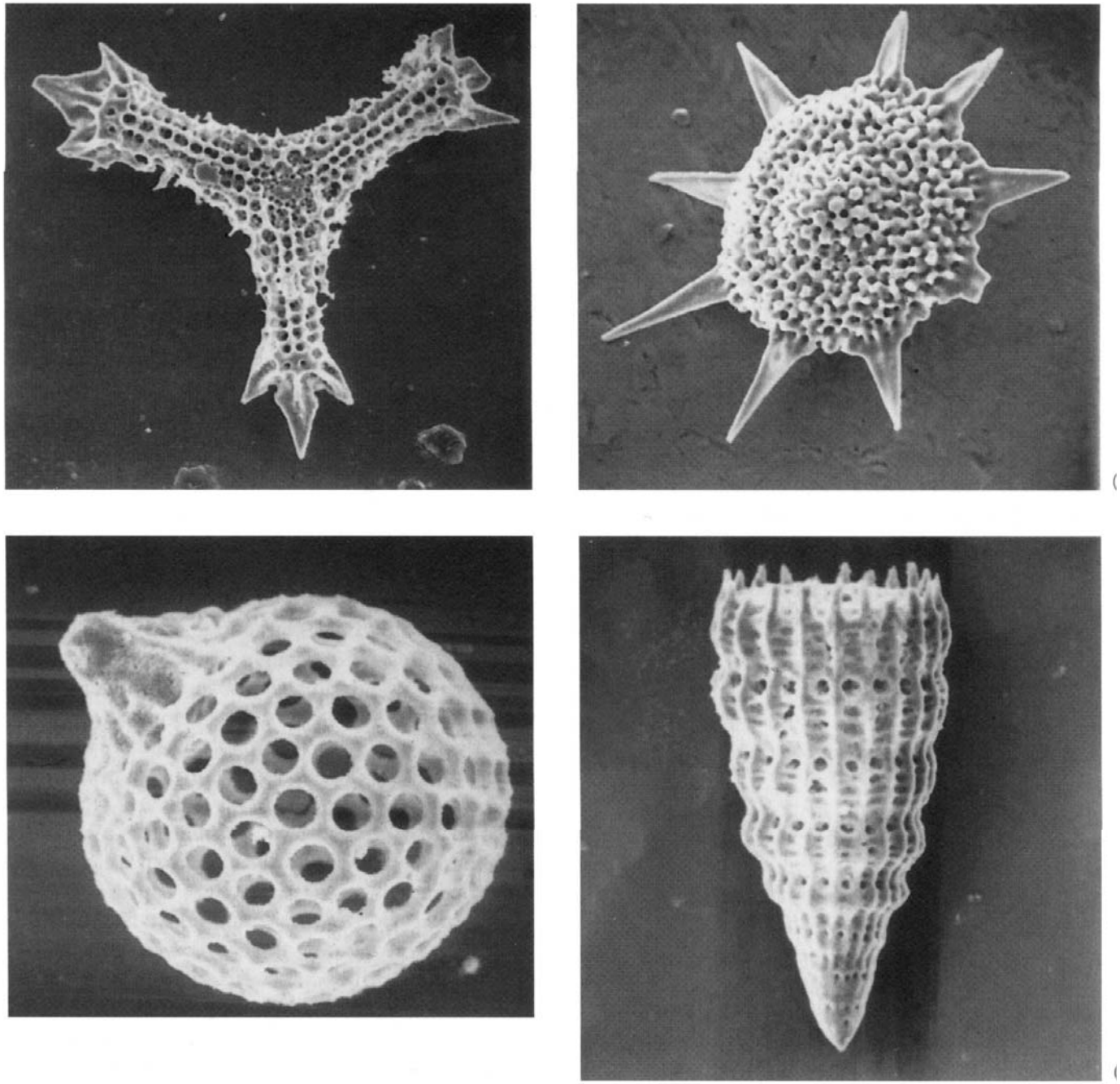
(a)
(c)

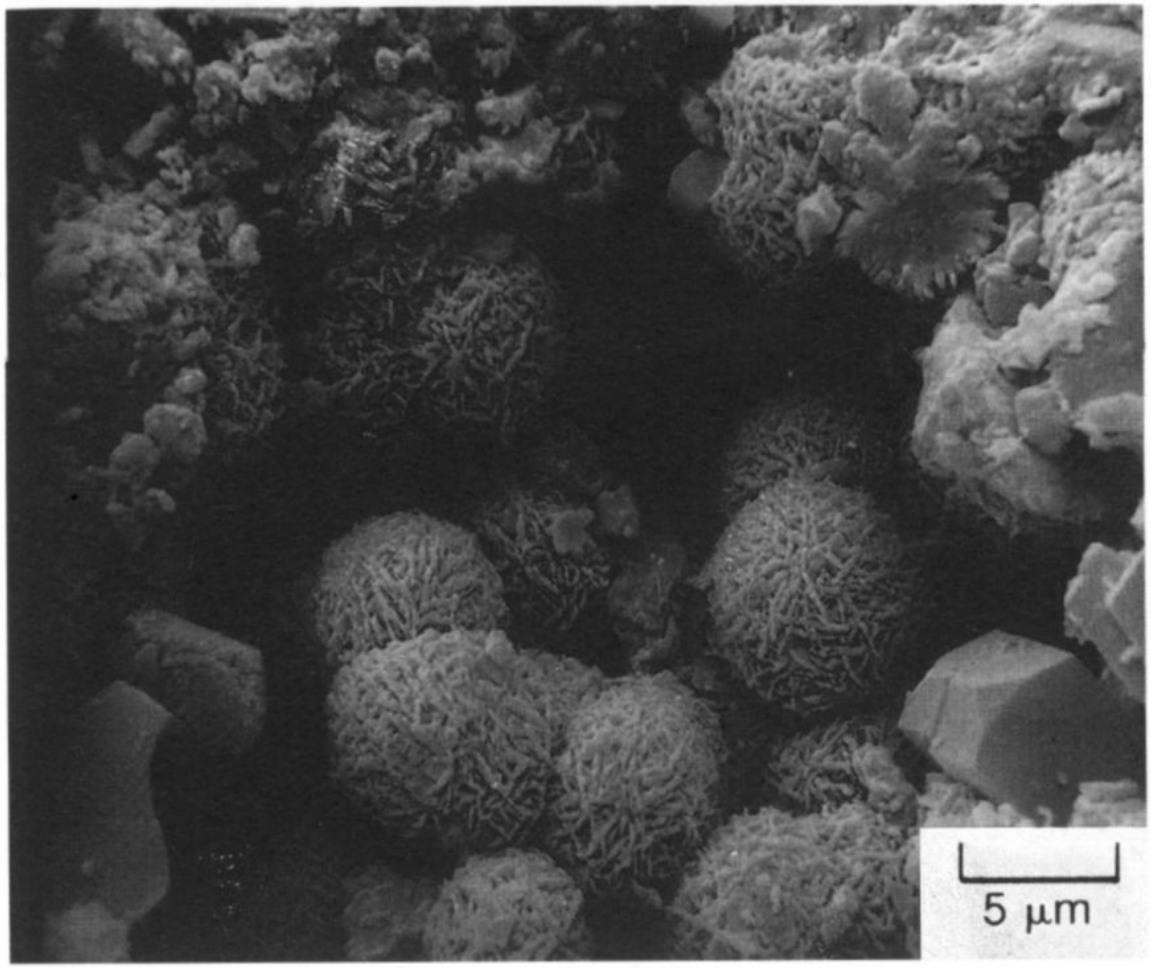


**Fig. 9.7** Lepispheres of opal-CT growing in voids in silicified Eocene chalk from the Arabian Sea. Sample from 630 m below sea floor. Prismatic crystals are clinoptilolite (a zeolite). Scanning electron micrograph.

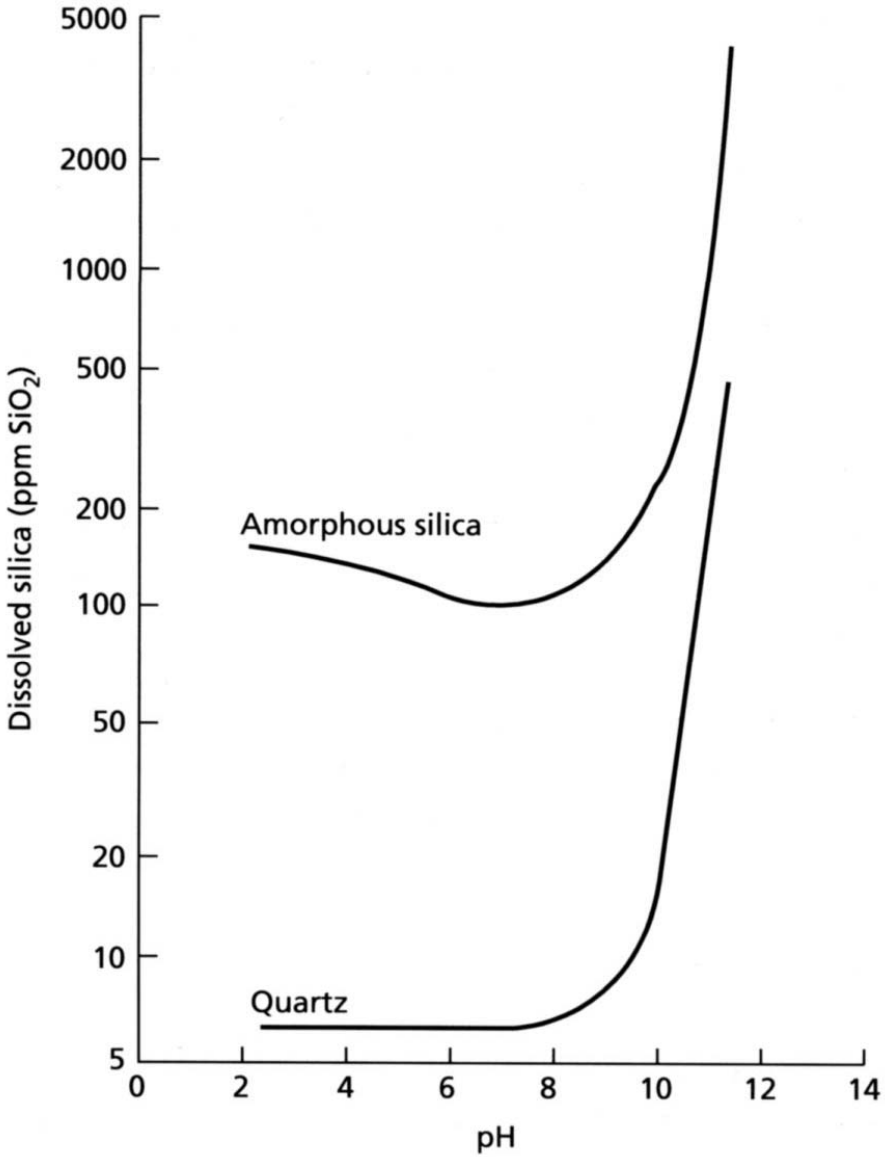


**Fig. 9.8** The solubility of quartz and amorphous silica at 25 °C. At pH values less than 9, the silica is in solution as undissolved orthosilicic acid ($H_4SiO_4$); above pH 9, this dissociates into $H_3SiO_4^{2-}$ and $H_2SiO_4^{2-}$.

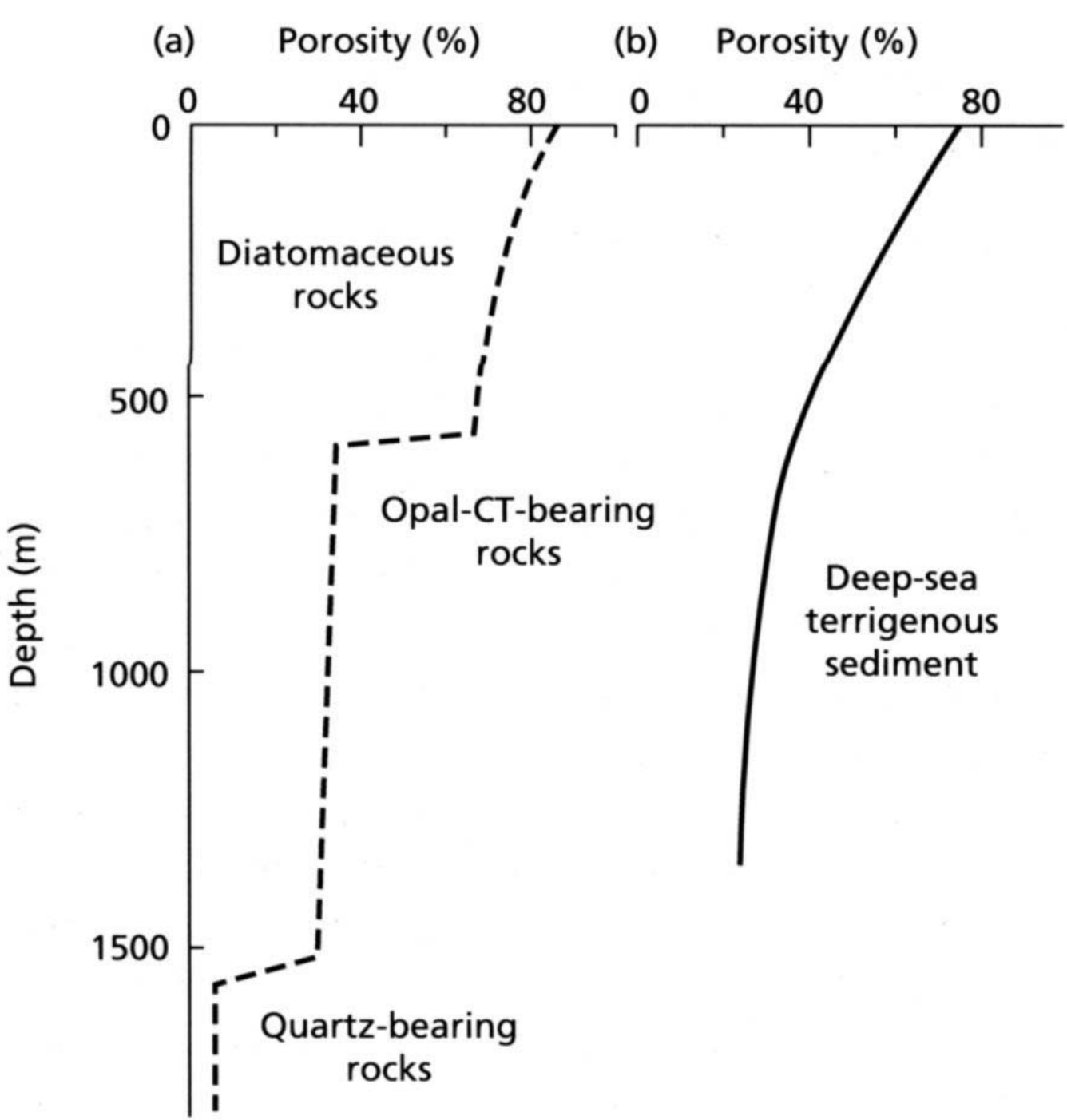
(a) Porosity (%)
0
40
80
0
(b) Porosity (%)
0
40
80
Depth (m)
500
1000
1500
Diatomaceous rocks
Opal-CT-bearing rocks
Quartz-bearing rocks
Deep-sea terrigenous sediment

# *Ferolity*

zdroje & transport Fe, eH-pH pole stability Fe ox.-hox.

raná diageneze

## glaukonit

granulární facie, impregnace, povlaky; autigenní Fe glaukonitický smektit, raně diag. Fe, K glaukonitická slída; řídící faktory : dostatek Fe, K, rovnováha mezi klastickým přínosem a vymýváním, nízká sedimentační rychlost ($10^3$ - $10^6$ let)

feromanganové nodule

**Table 6.1** The iron minerals of sedimentary rocks

| | |
|---|---|
| Oxides | hematite $\alpha$-$Fe_2O_3$ |
| | magnetite $Fe_3O_4$ |
| | goethite $\alpha$-FeO.OH |
| | limonite $FeO.OH.nH_2O$ |
| Carbonate | siderite $FeCO_3$ |
| Silicates | berthierine $(Fe_4^{2+}\ Al_2)\ (Si_2Al_2)\ O_{10}\ (OH)_8$ |
| | chamosite $(Fe_5^{2+}\ Al)\ (Si_3Al)\ O_{10}\ (OH)_8$ |
| | greenalite $Fe_6^{2+}\ Si_4\ O_{10}\ (OH)_8$ |
| | glauconite $KMg(FeAl)\ (SiO_3)_6.3H_2O$ |
| Sulphides | pyrite $FeS_2$ |
| | marcasite $FeS_2$ |

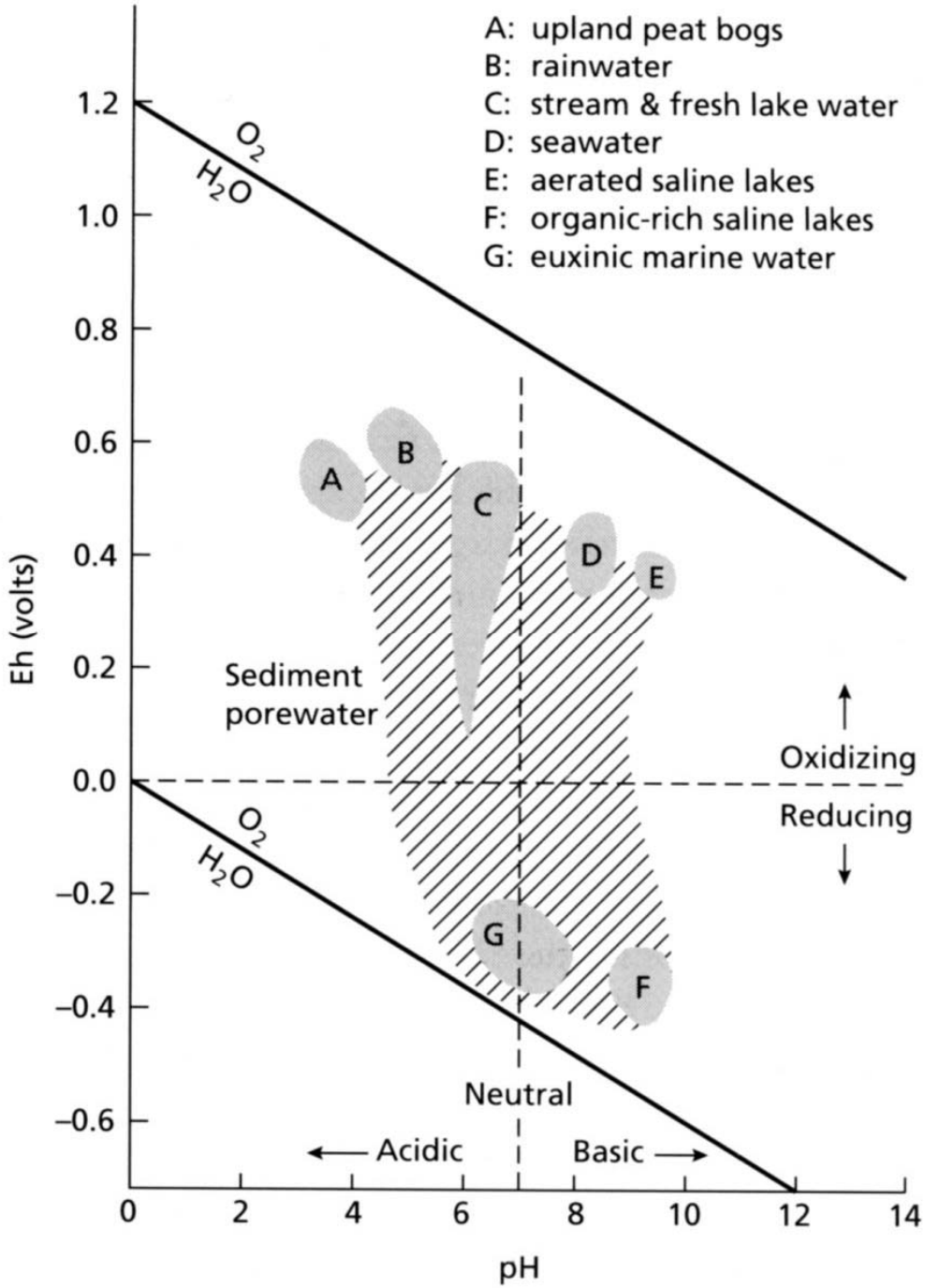
A: upland peat bogs
B: rainwater
C: stream & fresh lake water
D: seawater
E: aerated saline lakes
F: organic-rich saline lakes
G: euxinic marine water
1.2
1.0
0.8
0.6
0.4
0.2
0.0
–0.2
–0.4
–0.6
Eh (volts)
O2
H2O
O2
H2O
A
B
C
D
E
F
G
Sediment porewater
Oxidizing
Reducing
Neutral
Acidic
Basic
0
2
4
6
8
10
12
14
pH

**Table 6.2** Geochemical classification of early diagenetic environments and the characteristic phases present. After Berner (1981)

| Environment | Characteristic phases |
|---|---|
| *Oxic* | hematite, goethite, $MnO_2$-type minerals, no organic matter |
| *Anoxic* | |
| **1** sulphidic | pyrite, marcasite, rhodochrosite, organic matter |
| **2** non-sulphidic | |
| (a) post-oxic | glauconite, berthierine, no sulphide minerals, minor organic matter (also siderite, vivianite, rhodochrosite) |
| (b) methanic | siderite, vivianite, rhodochrosite, earlier formed sulphide minerals, organic matter |

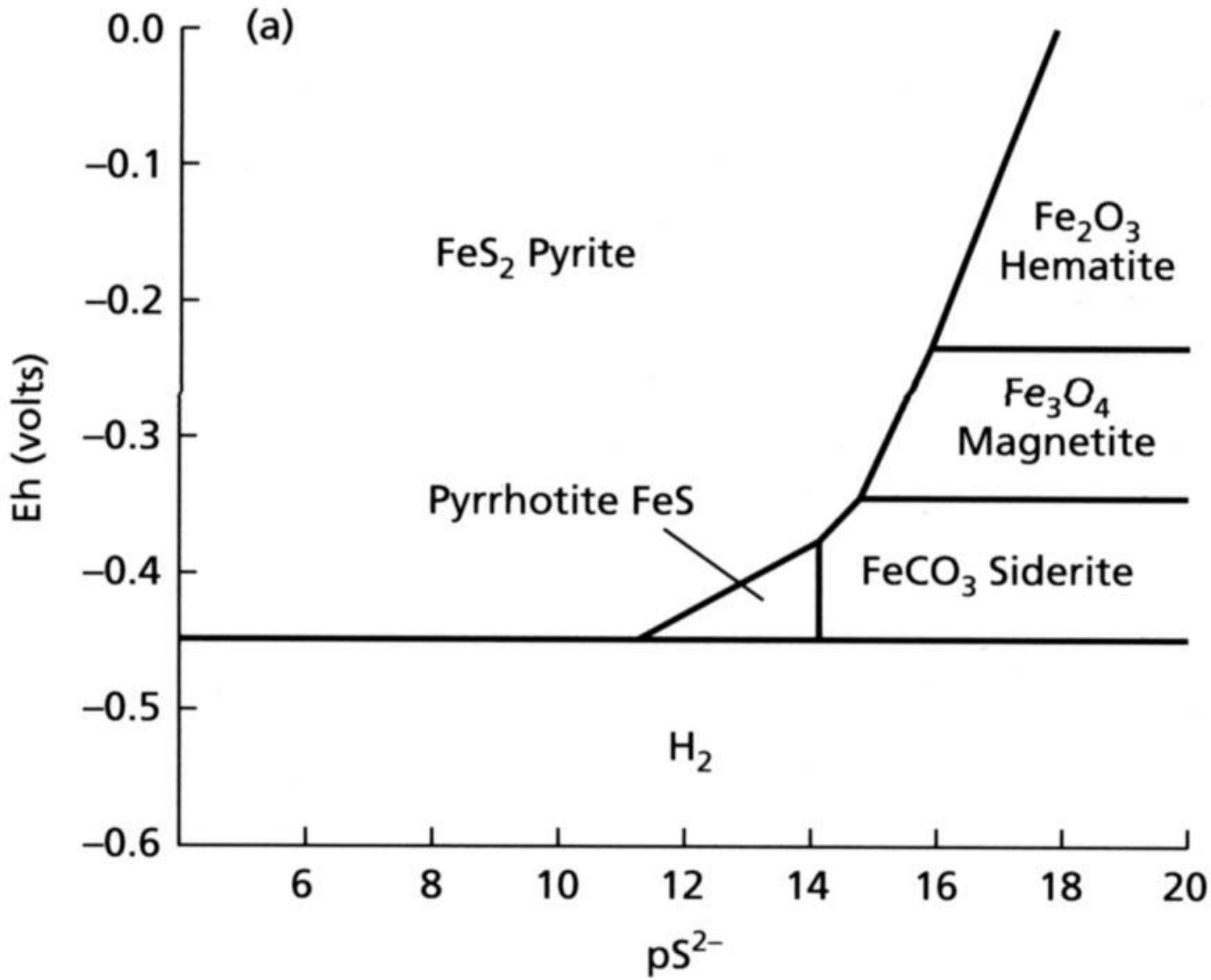
(a)
0.0
–0.1
–0.2
–0.3
–0.4
–0.5
–0.6
Eh (volts)
FeS2 Pyrite
Fe2O3 Hematite
Fe3O4 Magnetite
Pyrrhotite FeS
FeCO3 Siderite
H2
6
8
10
12
14
16
18
20
pS2–

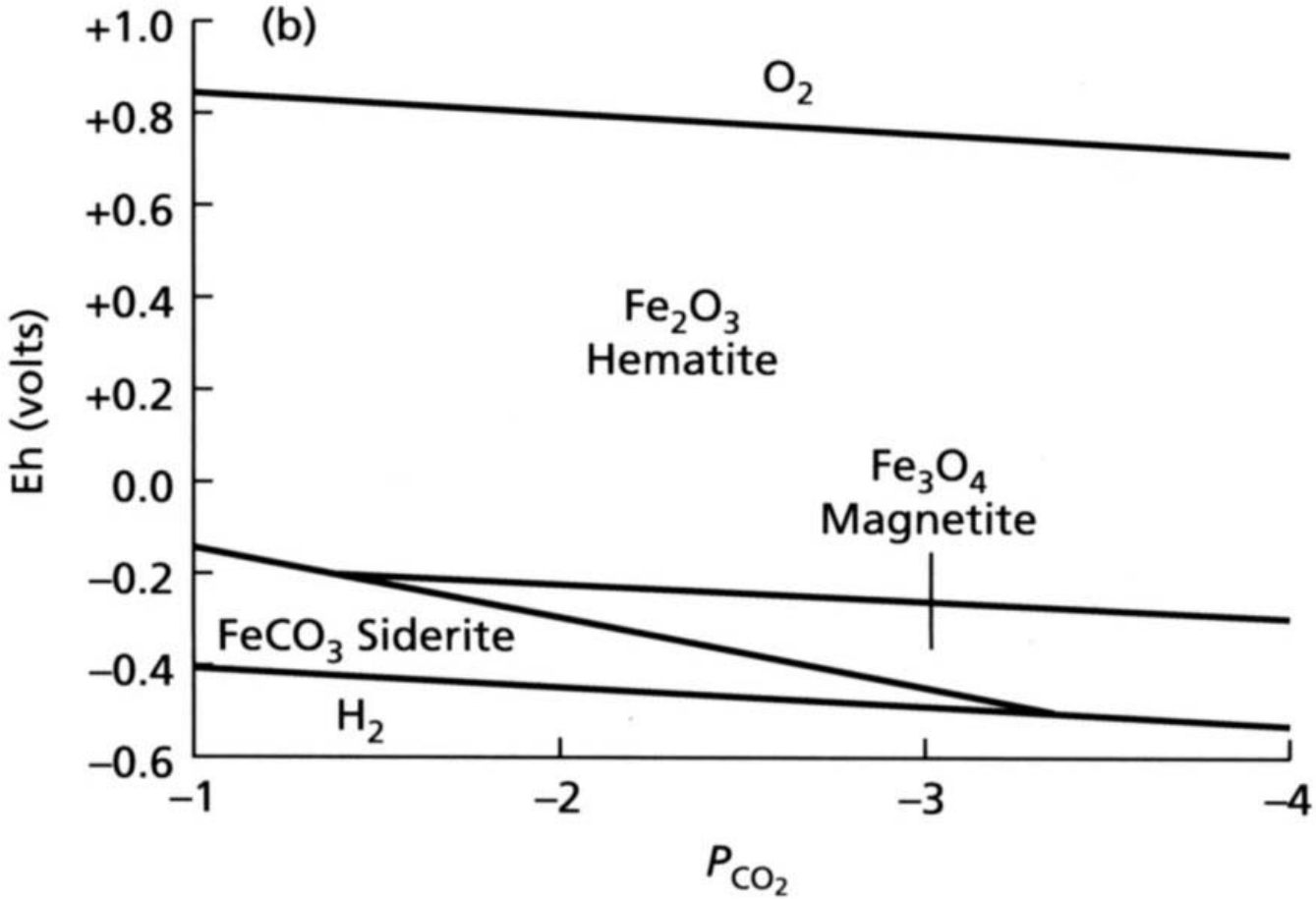


**Fig. 6.3** The stability fields of iron minerals plotted on (a) an Eh–$pS^{2-}$ diagram for a pH of 7.4 ($pS^{2-}$ is the negative log of the activity of the sulphide ion), and (b) an Eh–log $Pco_2$ diagram ($Pco_2$ is the partial pressure of $CO_2$). In the latter case, the value of $pS^{2-}$ is assumed to be so high (i.e. the activity of sulphur is very low), that pyrite and pyrrhotite do not plot on this diagram.

**Table 6.3** Average concentration of Fe, Mn, Cu, Co and Ni (in percentages) of shallow- and deep-water sediments and ferromanganese nodules from three sea-floor settings. From Glasby (1977)

| | Nearshore sediments | Deep-sea sediments, Atlantic | Seamount nodules | Abyssal nodules | Active ridge nodules |
|---|---|---|---|---|---|
| Fe | 4.83 | 5.74 | 15.81 | 17.27 | 19.15 |
| Mn | 0.0850 | 0.3980 | 14.62 | 16.78 | 15.51 |
| Cu | 0.0048 | 0.0115 | 0.058 | 0.37 | 0.08 |
| Co | 0.0013 | 0.0039 | 1.15 | 0.256 | 0.40 |
| Ni | 0.0055 | 0.0079 | 0.351 | 0.54 | 0.31 |
| Depth | | | 1900 m | 4500 m | 2900 m |

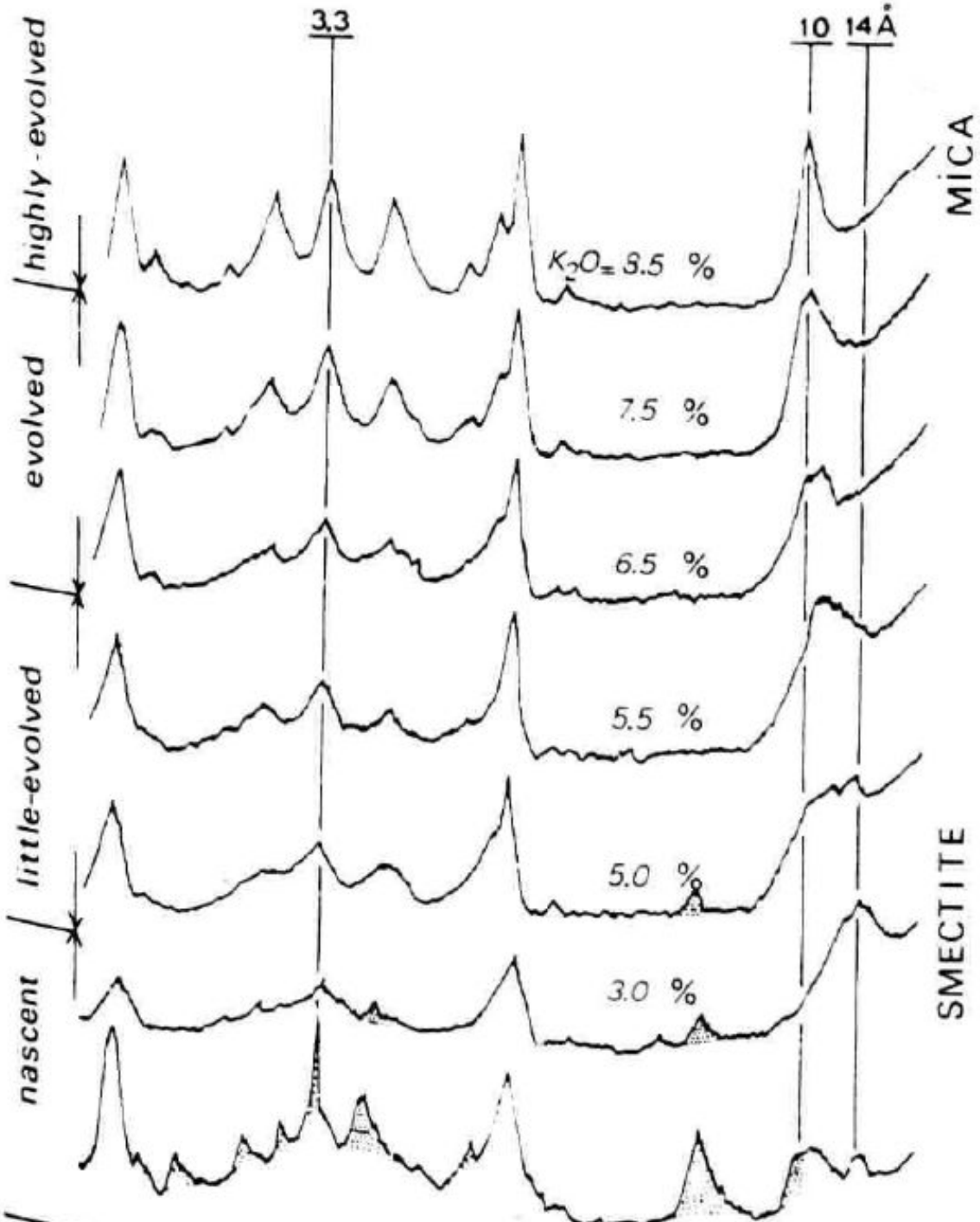
3.3
10
14 Å
highly-evolved
evolved
little-evolved
nascent
$K_2O$= 8.5 %
7.5 %
6.5 %
5.5 %
5.0 %
3.0 %
MICA
SMECTITE

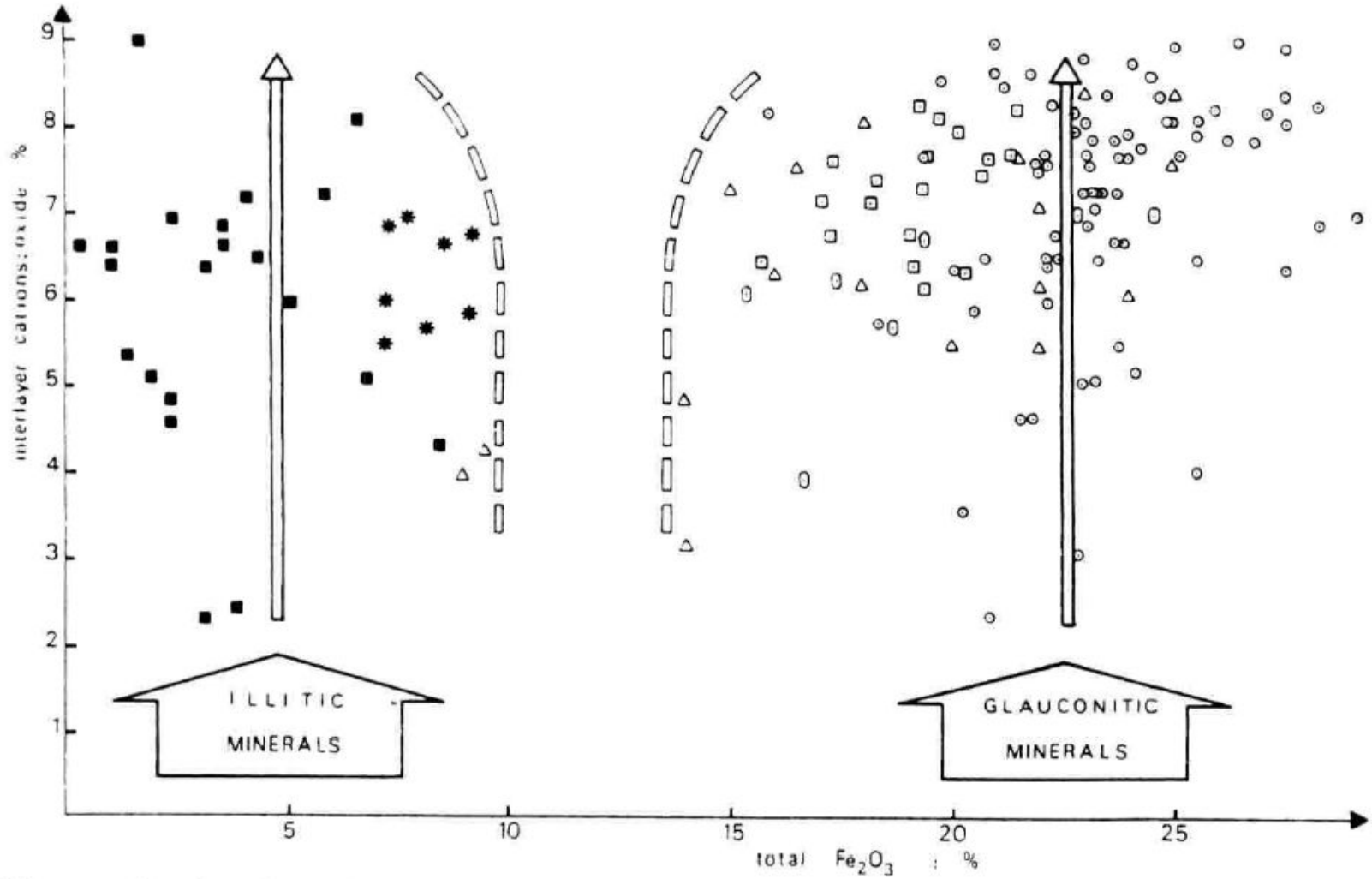


**Fig. 8.** Diagram showing the position of the illitic and the glauconitic mineral families with respect to their iron and interlayer cation content. Data from ○ Table 1, ⊡ Cimbalnikova (1971a), ⊙ Parry & Reeves (1966), △ Hower (1961) —these samples appear to be mixtures of clay minerals of authigenic and of substrate origin—★ Kossovskaya & Drits (1970), ■ Hower & Mowatt (1966). Lack of values between about 10–15% $Fe_2O_3$ suggests absence of a mineralogical transition between illitic and glauconitic minerals. Arrows show evolution from a smectitic to a mica-type clay mineral within both families. Glaucony does not increase in iron content with increasing amounts of interlayer cations.

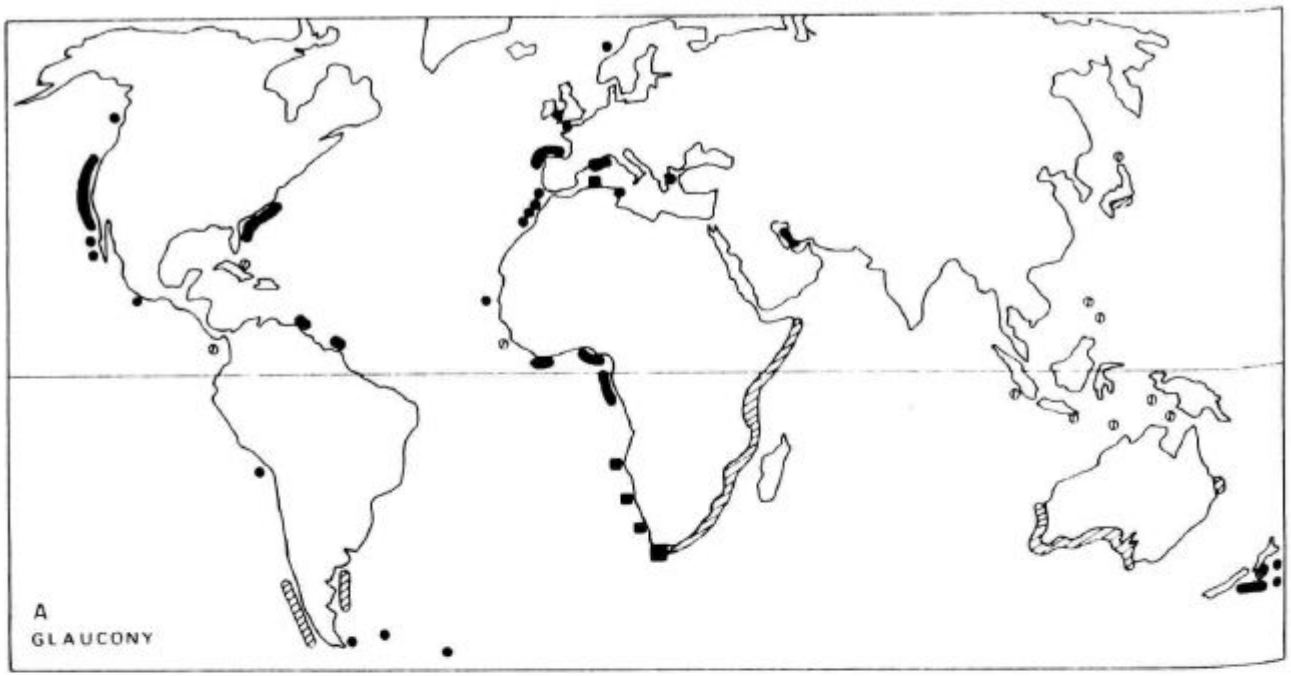
A
GLAUCONY

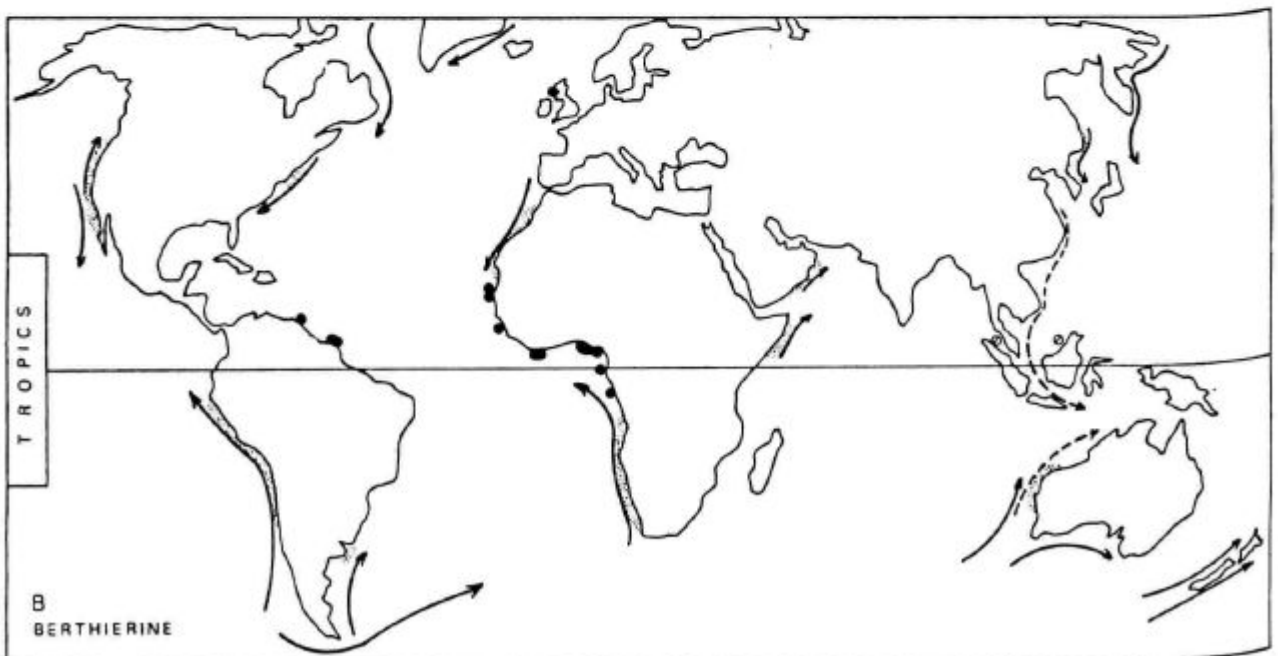
TROPICS
B
BERTHIERINE

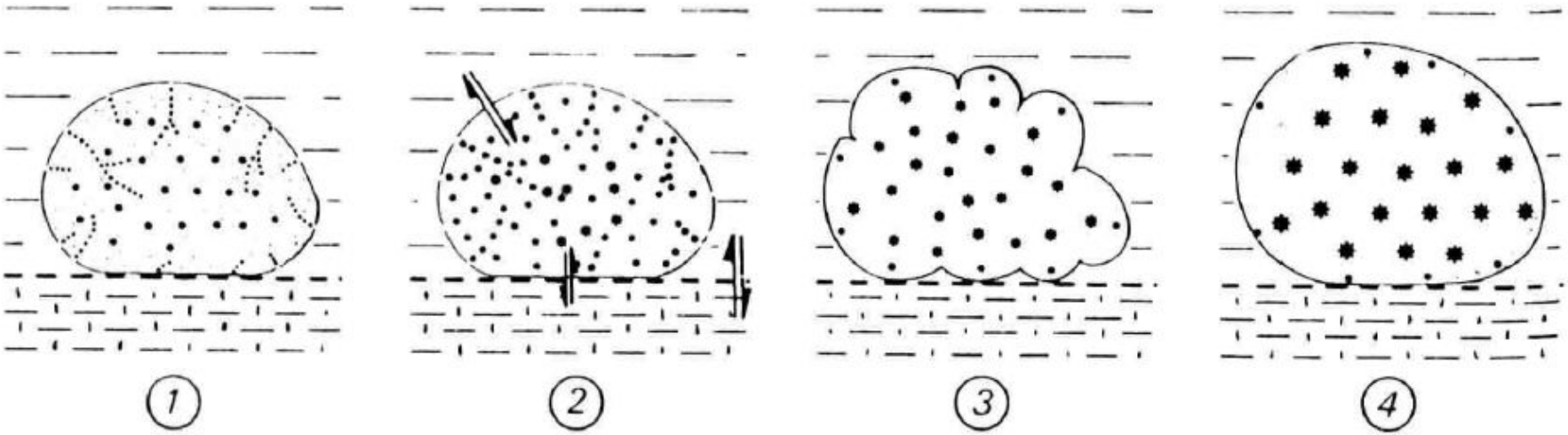


**Fig. 12.** Schematic representation of the evolution of a grain during glauconitization. Four stages from nascent (1) to highly-evolved (4) are selected from the continuum of changes observed in grains from the present shelf floor. Asterisks represent growth of glauconitic minerals. For discussion, see text.

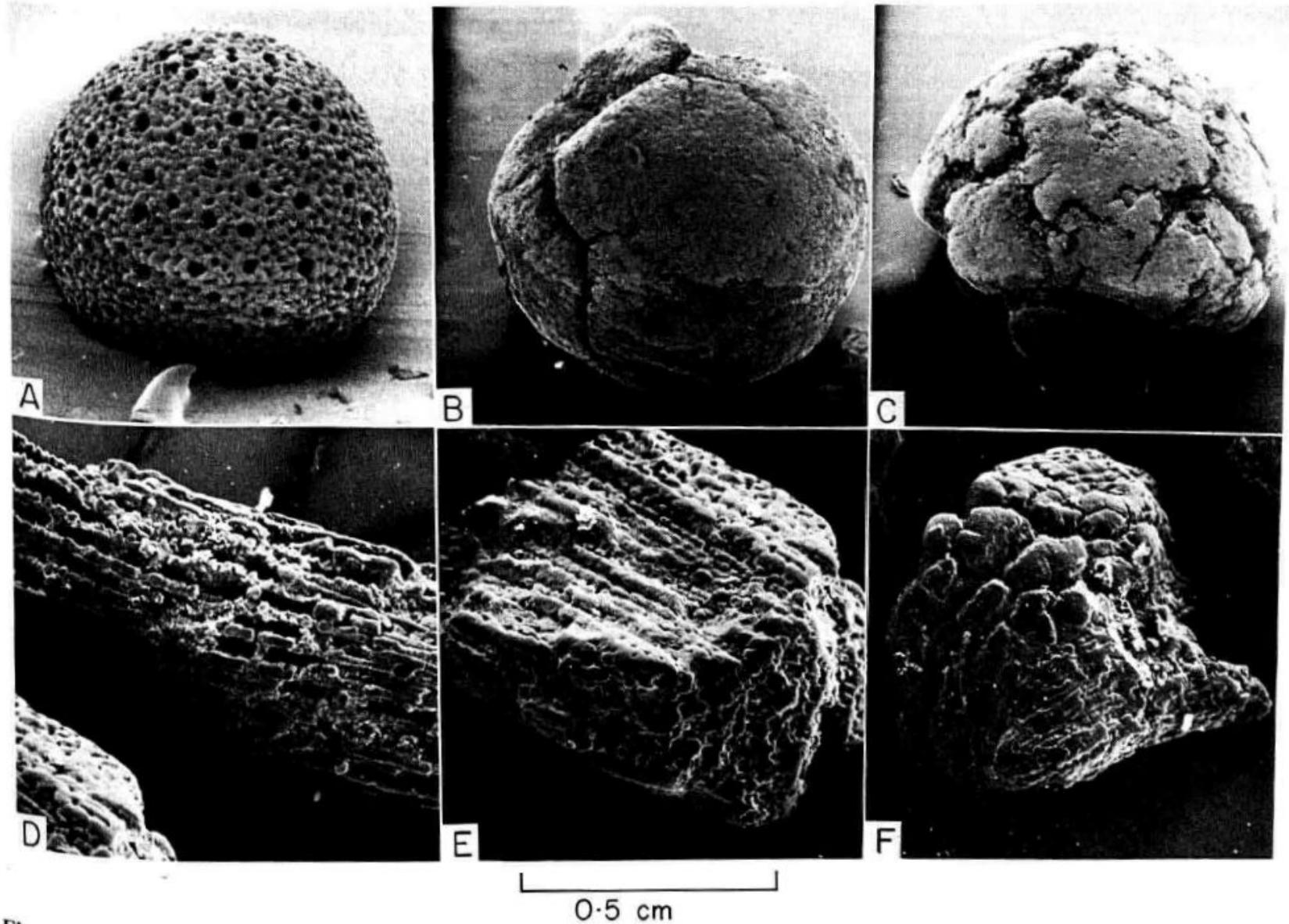


Fig. 15. SEM photomicrographs of Orbulina tests (A, B, C) and echinoderm fragments (D, E, F) showing progressive deformation during glauconitization. (A) Orbulina with pale green interior; (B) green mould with development of cracks; (C) dark green mould with large cracks leading eventually to splitting. Sequence (D) to (F) shows loss of original texture of echinoderm stereom during replacement by authigenic glauconitic crystals and development of a typical cracked grain.

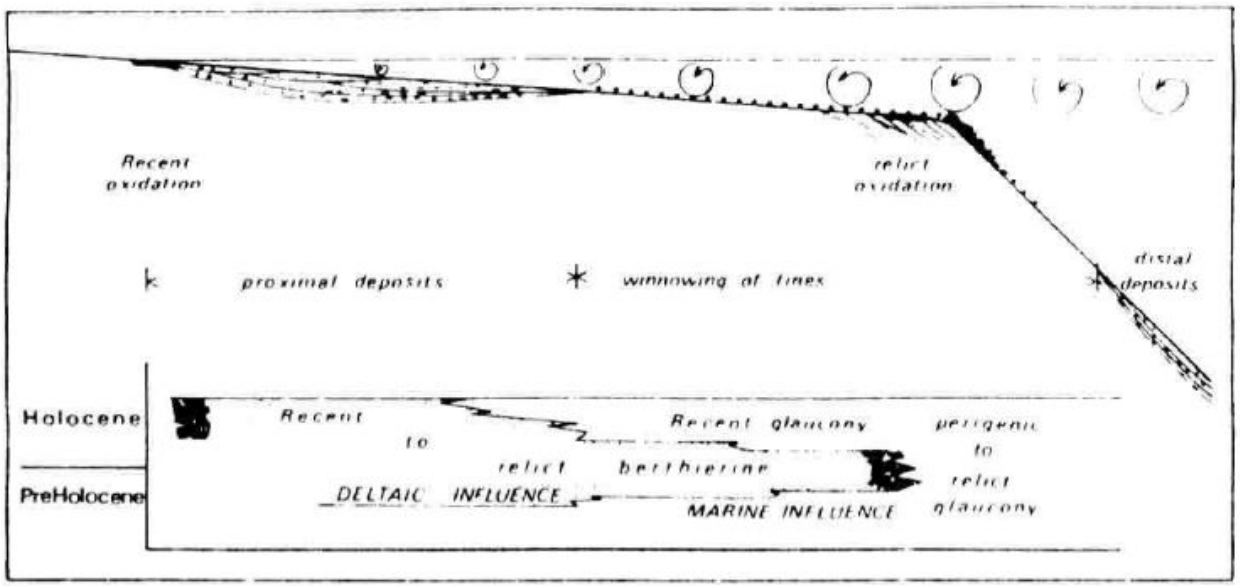


**Fig. 18.** Schematic diagram showing the environments of formation of glaucony and berthierine as a function of detrital influx and energy levels on a passive continental margin. Cross-section below shows facies relationships of glaucony and berthierine as a result of the Holocene transgression.

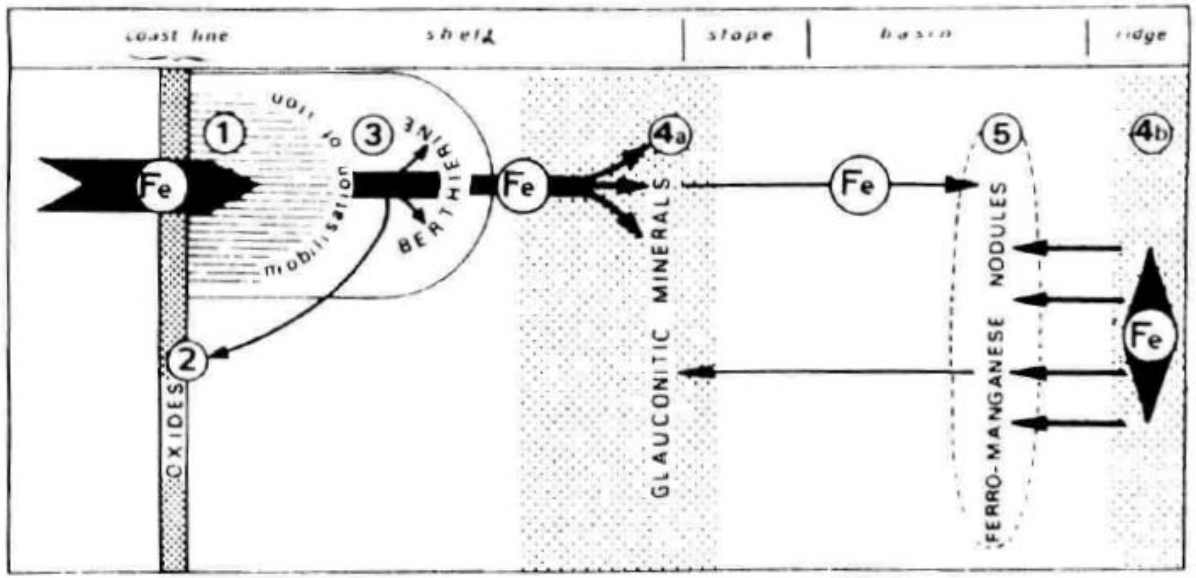


**Fig. 19.** Position of green sheet silicates in the geochemical path of iron in the sea. Zone 1, accumulation of detrital iron; zone 2, chemical precipitation of iron and oxidation of detrital iron minerals; zone 3, authigenic growth of berthierine; zones 4a, b, authigenic growth of glauconitic minerals; zone 5, growth of ferromanganese nodules. Modified from Odin (1975b).

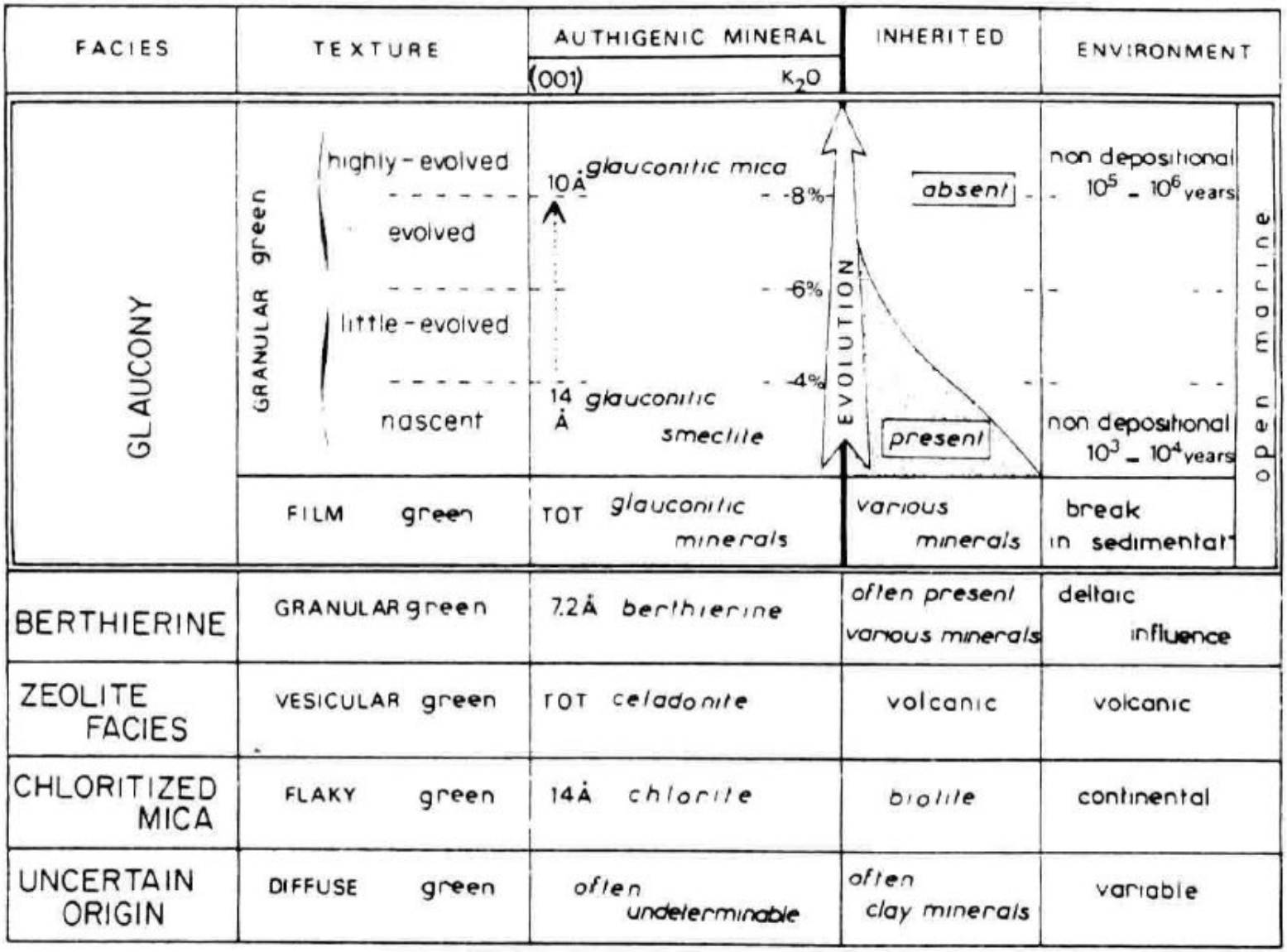


**Fig. 20.** Genetic classification of glaucony and related facies.

hematitový ferolit

(c)

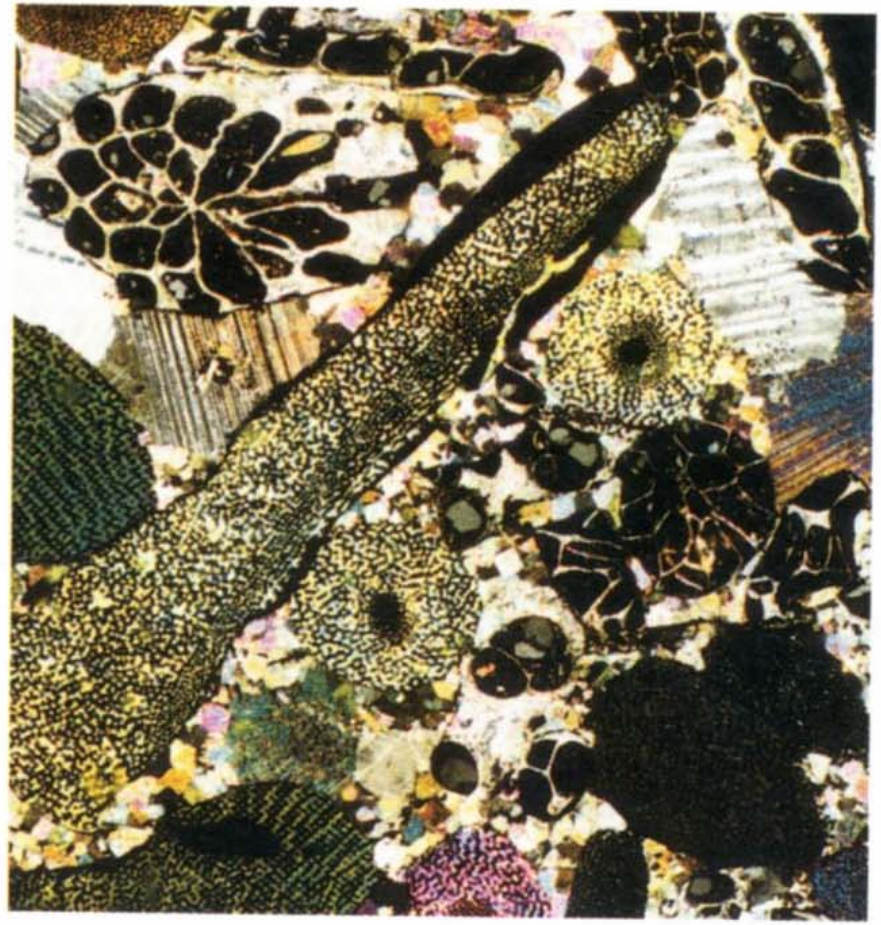

(d)

krinoidi, mechovky

chamozitový ferolit
ooidy

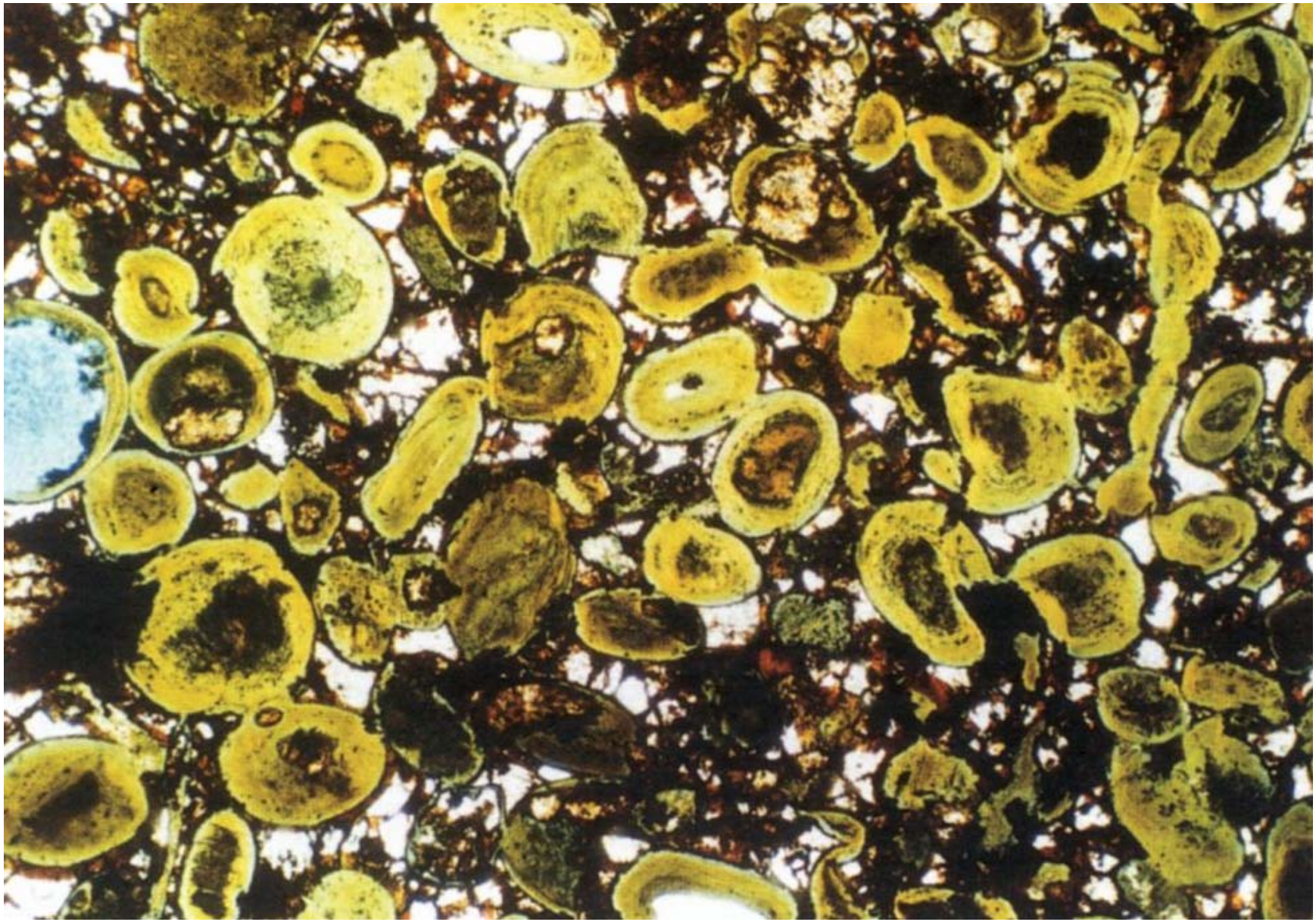

berthierit, chamozit, siderit, goethit

# *Fosfáty*

mineralogie (karbonát fluorapatit - CFA, frankolit, alophan)

distribuce recentních výskytů

genetické modely marinních fosfátů - upwelling, ostrovy, atoly, podmořské hory, guyoty, epeirická prostředí

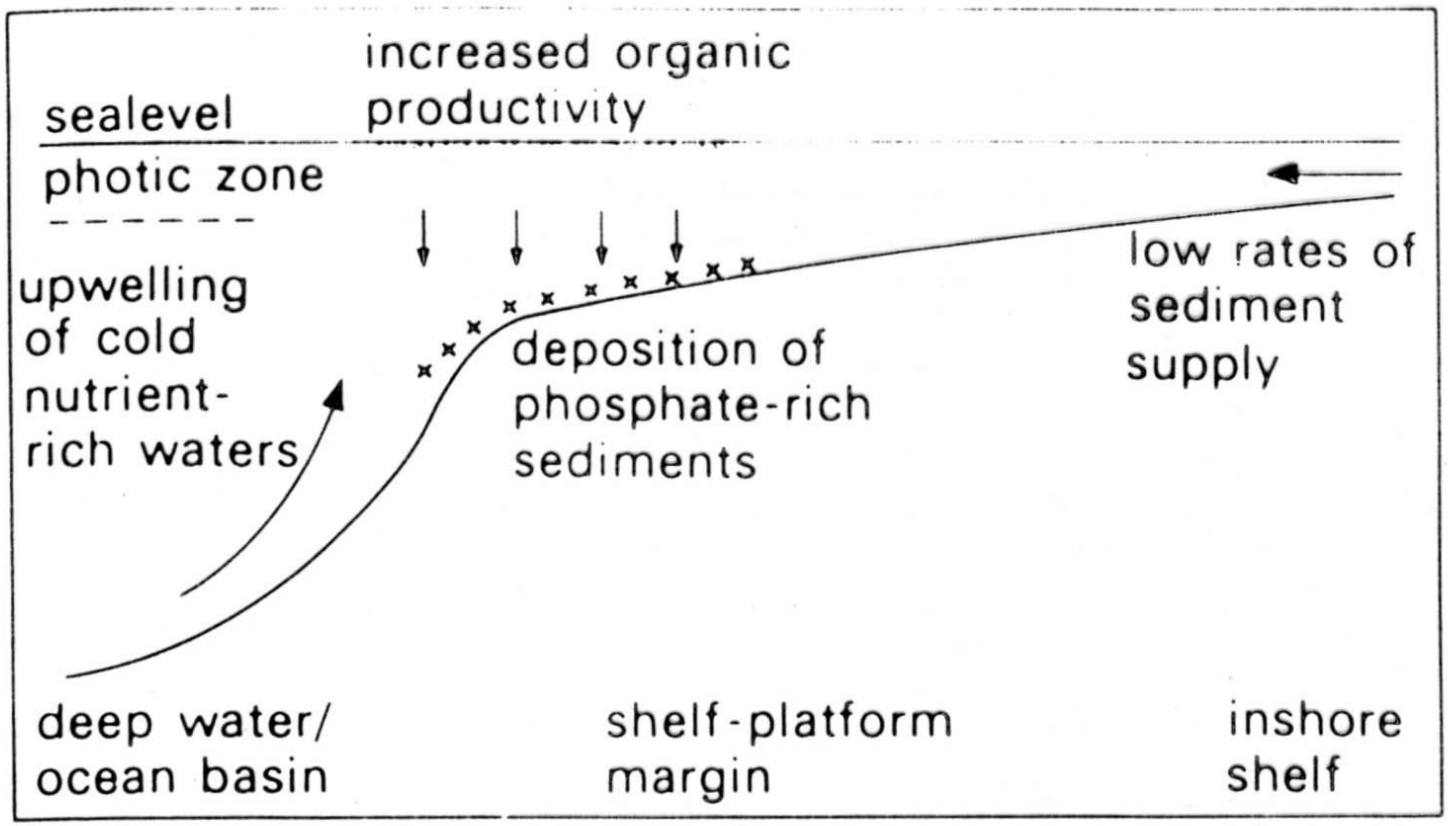


**Fig. 7.2** Model for formation of marine phosphorites.

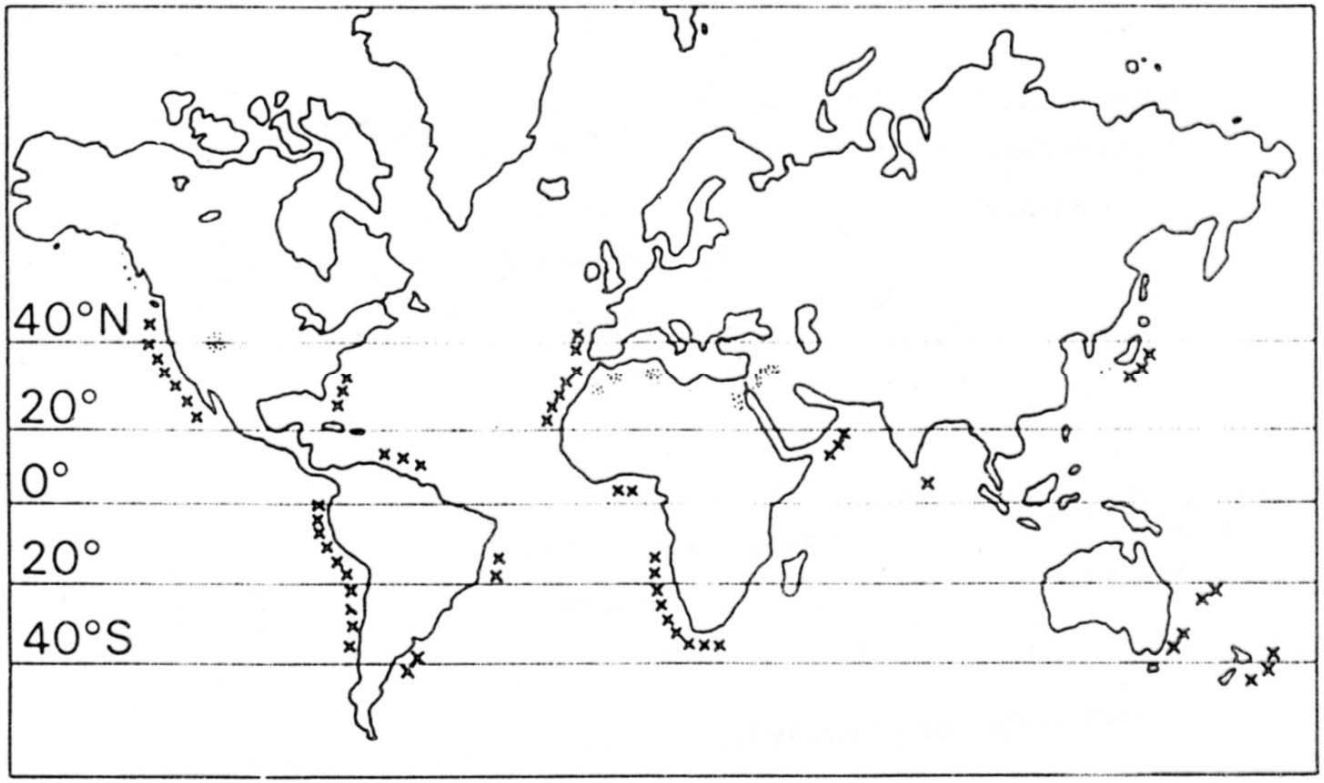


**Fig. 7.1** Distribution of marine phosphorites, although in many cases the deposits are not actually forming at the present time. Also shown are the locations of the Permian Phosphoria Formation of northwestern USA and the Cretaceous–Tertiary phosphorites of the Middle East–North Africa.

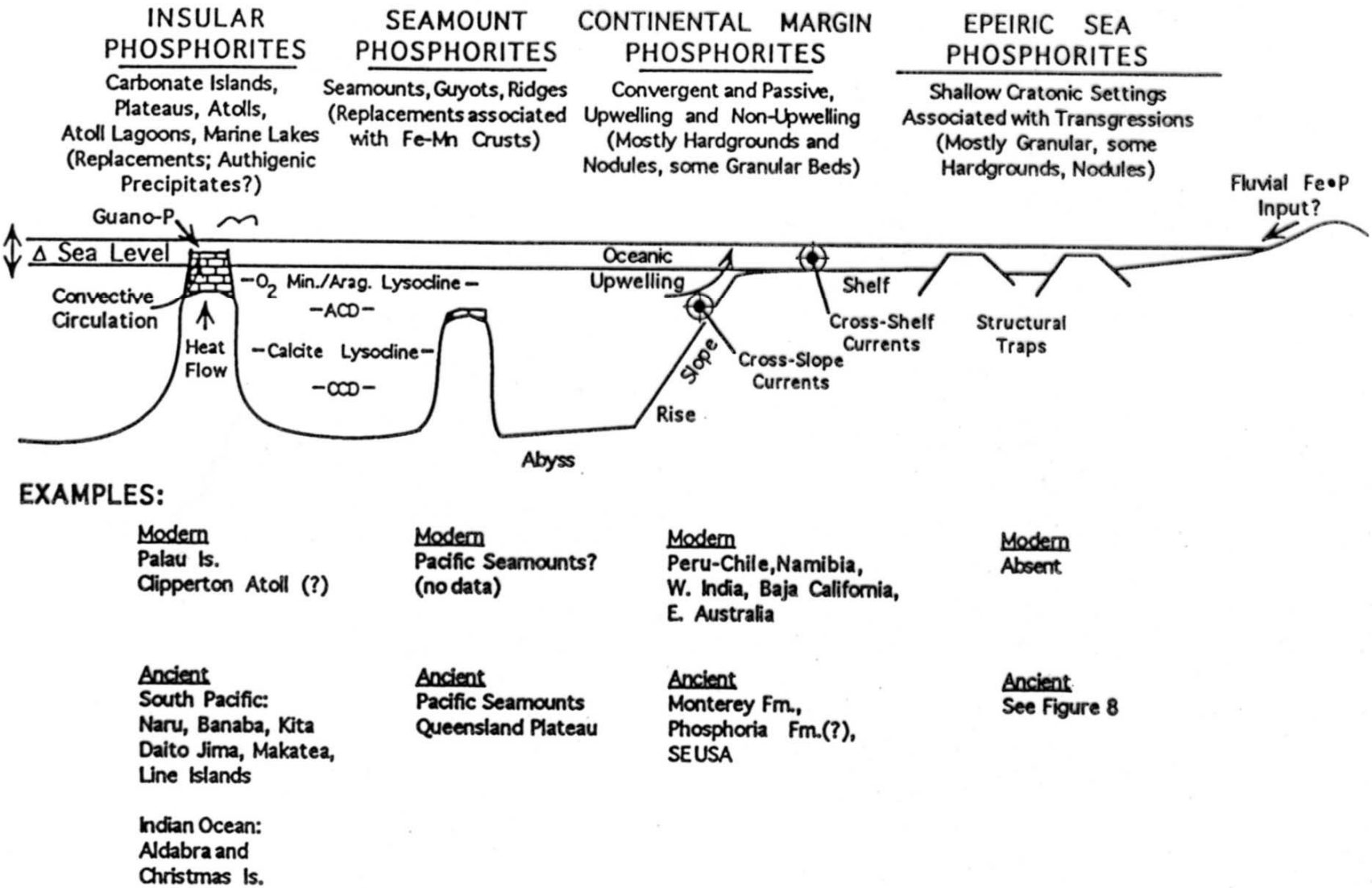


Fig. 1. Tectonic and oceanographic settings of marine phosphorites as derived from studies of the modern and ancient record.

1. *F-phosphates:* small nodules, peloids or laminae of *friable,* light colored CFA. These were called collophane mudstones by Burnett et al. (1980). Consistency varies from very friable and unconsolidated to more compact, though even the latter can be scratched with a fingernail. Presumably, F-phosphates age or mature to eventually become D-phosphates.
2. *D-phosphates:* well lithified, often dark and dense nodules, gravels and hardgrounds of CFA.
3. *P-phosphates:* phosphoritic sands dominated by structureless and coated (microbanded) phosphatic grains, with some admixtures of fish bones and teeth.

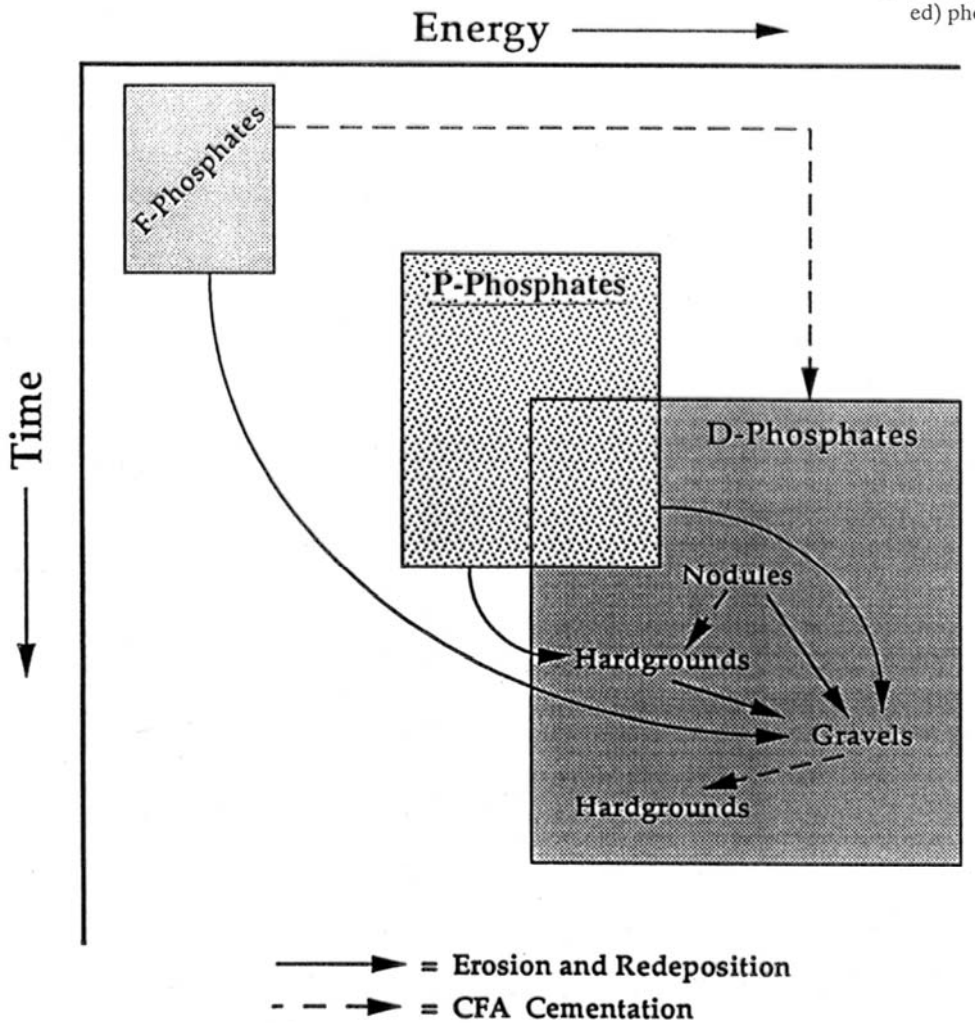


Fig. 2. Schematic portrayal of energy and time relationships for the formation and evolution of F-, P-, and D-phosphates. Shown also are the transitions among the three kinds of phosphorites that result from reworking and carbonate fluorapatite cementation on or near the sea floor. Modified from Garrison & Kastner 1990.

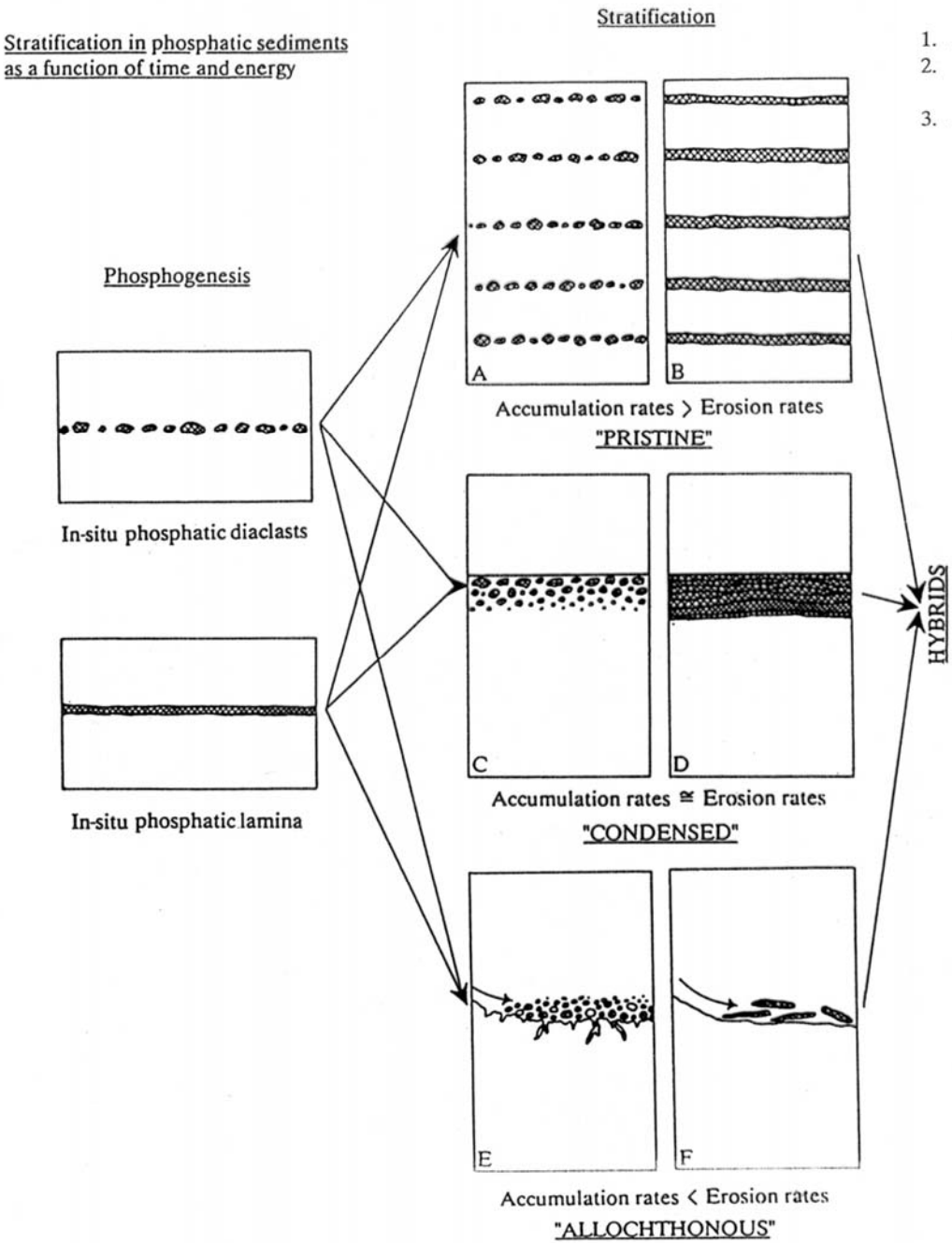


1. ***Pristine:*** phosphates which lack any signs of reworking.
2. ***Condensed:*** phosphatic laminae and particles which have concentrated by winnowing processes or bioturbation.
3. ***Allochthonous:*** phosphatic particles that have been entrained by and redeposited from turbulent and/or gravity-driven flows.

Fig. 3. Genetic classification of stratification types in phosphorites. From Föllmi et al. 1991, reprinted with permission of Springer-Verlag.

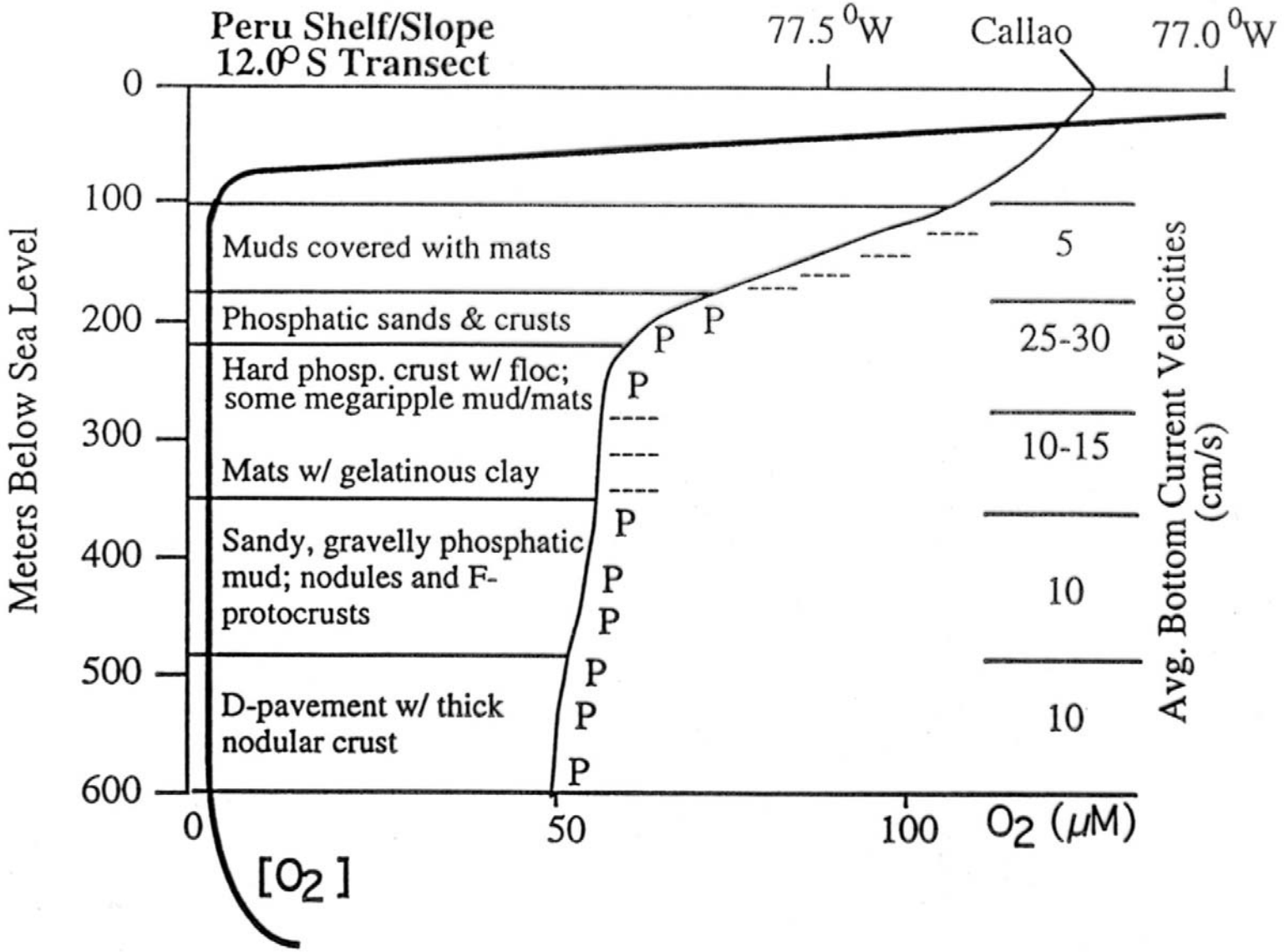
Peru Shelf/Slope
12.0° S Transect
77.5 °W
Callao
77.0 °W
0
100
200
300
400
500
600
Meters Below Sea Level
Muds covered with mats
Phosphatic sands & crusts
Hard phosp. crust w/ floc;
some megaripple mud/mats
Mats w/ gelatinous clay
Sandy, gravelly phosphatic
mud; nodules and F-
protocrusts
D-pavement w/ thick
nodular crust
P
5
25-30
10-15
10
10
Avg. Bottom Current Velocities
(cm/s)
0
50
100
O2 (μM)
[O2]

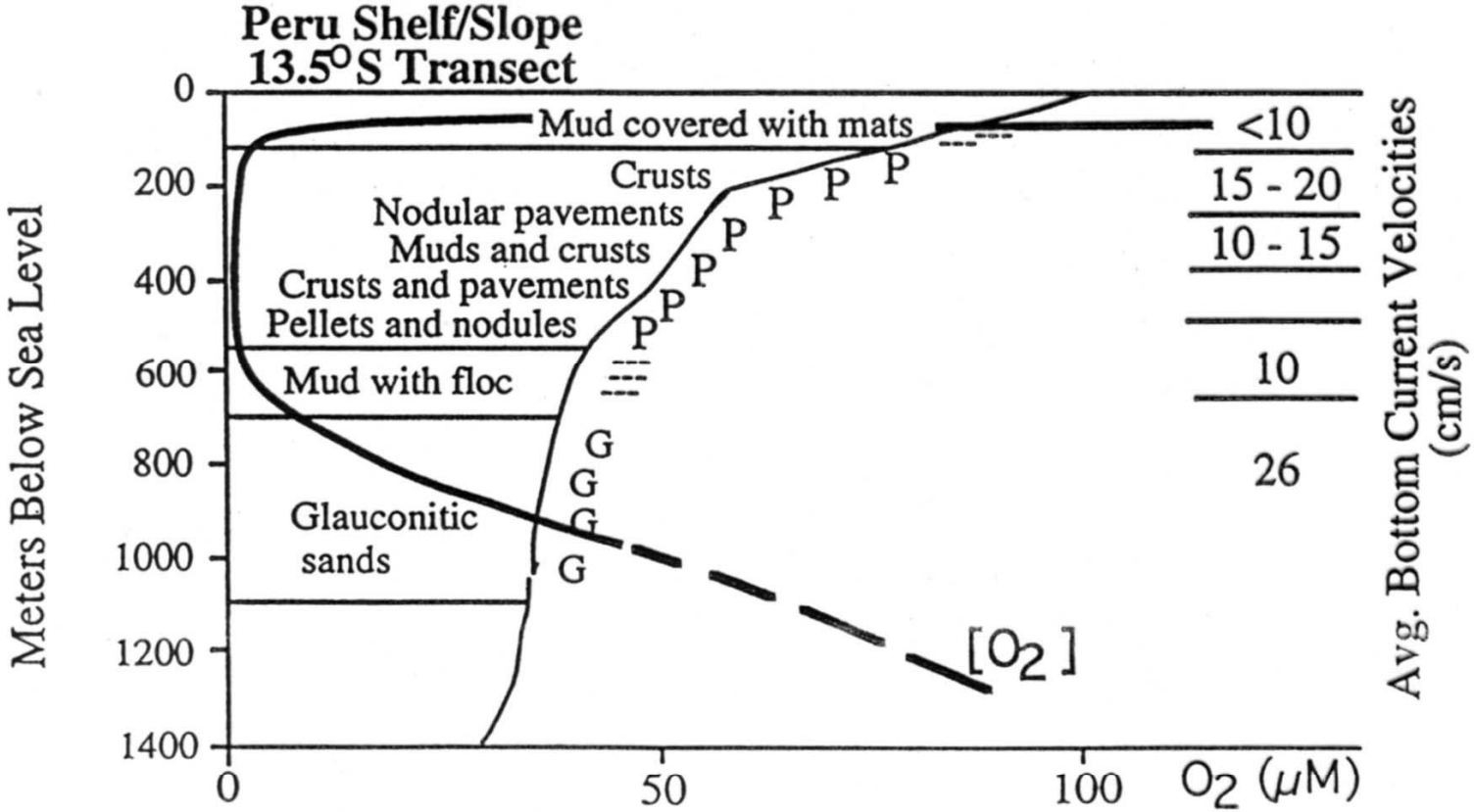


Fig. 5. Sediment and phosphorite distribution together with measured bottom current velocities (cm/s) and dissolved oxygen concentrations (μM) on the outer Peru shelf and upper slope at 12°S (top) and 13.5°S (bottom) (results from R/V *Seward Johnson,* 1992 cruise; unpublished). "P" represents distribution of phosphorite. Nodular hardground pavements and phosphatic sands occur in association with highest current velocities. Friable (F-phosphate) CFA-protocrusts occur between about 350 and 500 m. Glauconitic sands occur along the base of the oxygen minimum zone between 700 m and 1100 m at 13.5°S. Bacterial mats are sulfide-oxidizing *Thioploca* sp. After Glenn et al. 1994.

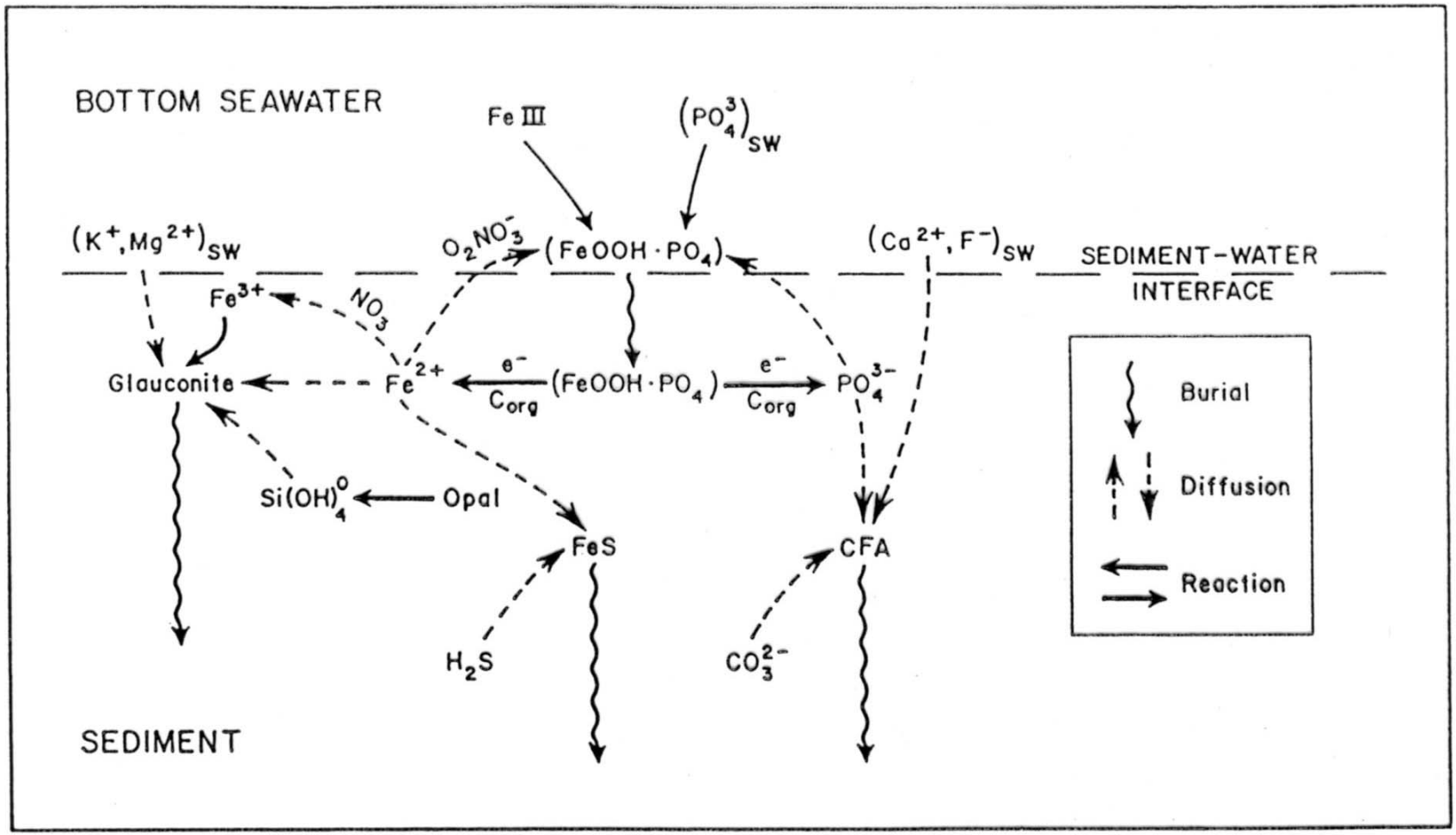


Fig. 6. Schematic diagram of iron redox-P cycle as postulated for Peru Margin sediments by Froelich et al. (1988). Iron hydroxyoxides sorb phosphate from bottom water and from upward diffusing pore water phosphate. Once reduced below the sediment-water interface these compounds release the sorbed phosphate to pore waters which is then precipitated. The reduced iron ($Fe^{2+}$) fluxes back to the more oxidizing environment of the bottom waters, where it may again sorb phosphate, or is precipitated in the sediments as a component of pyrite or glauconite. A somewhat similar mechanism has also been proposed for the modern sediments of the east Australian margin (see text). Reprinted with permission of Elsevier Science.

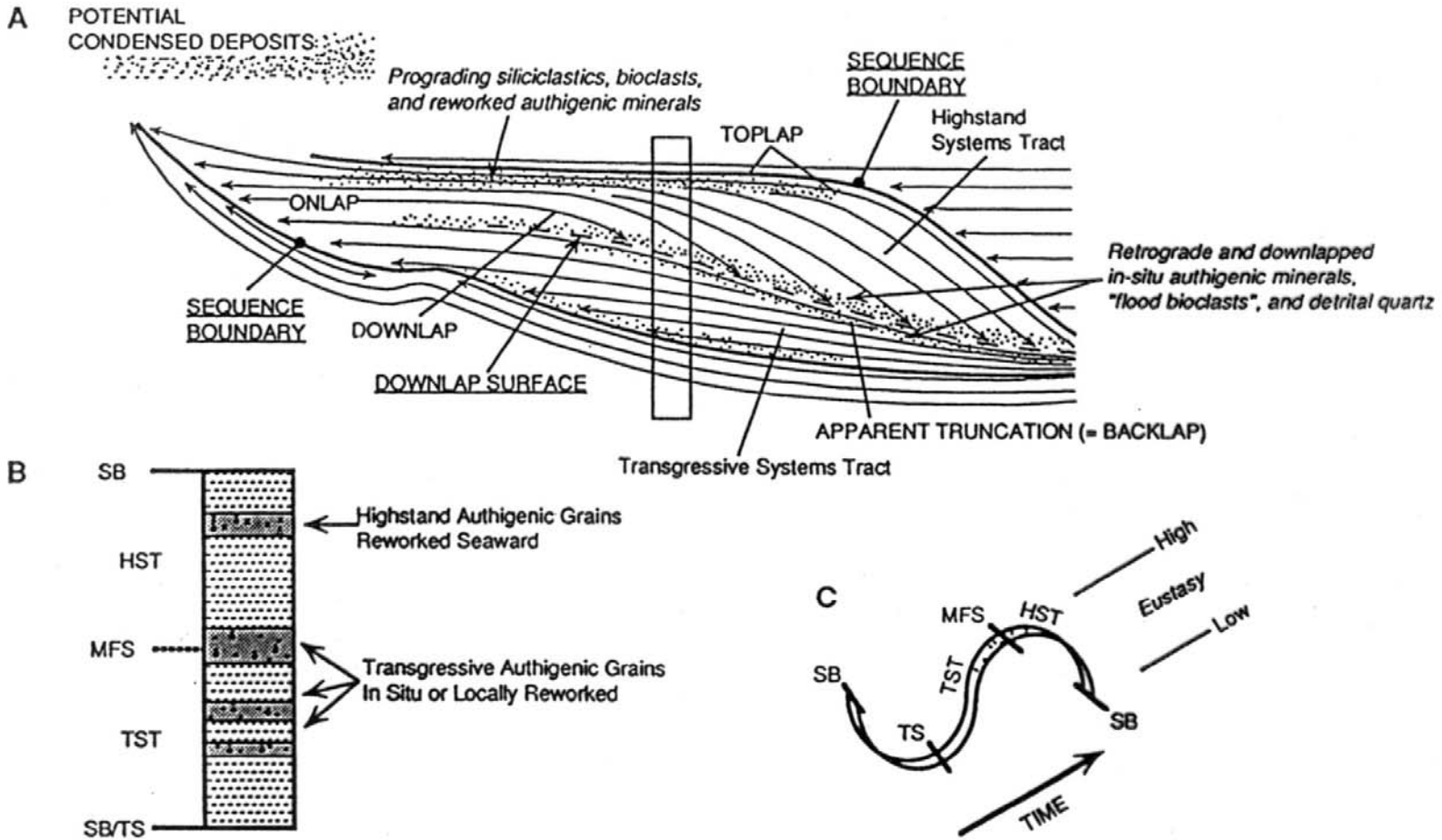


Fig. 10. Potential relationships between sequence stratigraphy, condensed sections and phosphorites. (**A**) Possible positions of sequence condensation within an idealized depositional sequence (stipples), (after Kidwell 1991). (**B**) Schematic illustration of the placement of non-reworked pristine authigenic phosphorite (and/or glauconite) and reworked phosphorite (and/or glauconite). Pristine phosphates may form within transgressive systems tracts and at the maximum flooding surface, whereas later phases are reworked seaward within highstand systems tracts. (**C**) The timing of systems tracts development with respect to one cycle of sea level change. LST = lowstand systems tract, TST = transgressive systems tract, HST = highstand systems tract, TS = transgressive surface, MFS = maximum flooding surface, SB = sequence boundary. Dots on the sea level curve represent locations of maximum phosphorite emplacement. After Glenn & Kronen 1993.

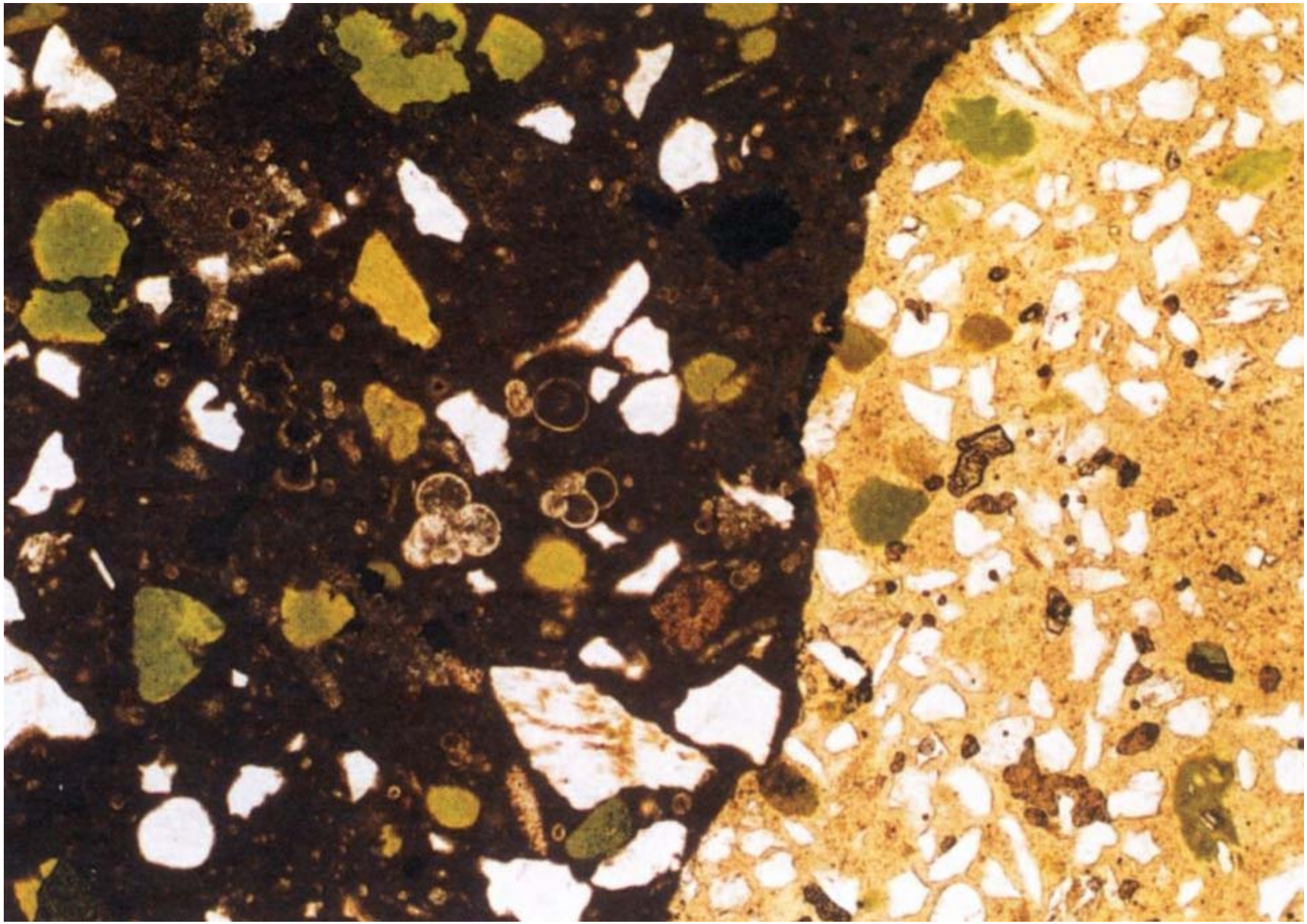

glaukonit, fosfát

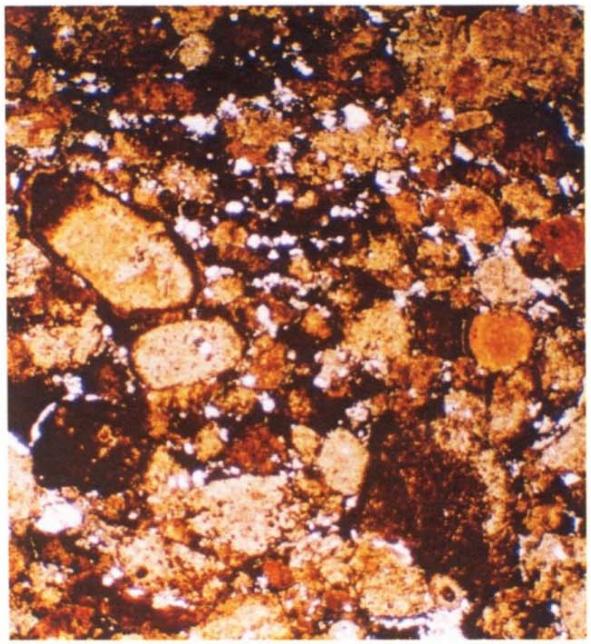

(c)

(d)

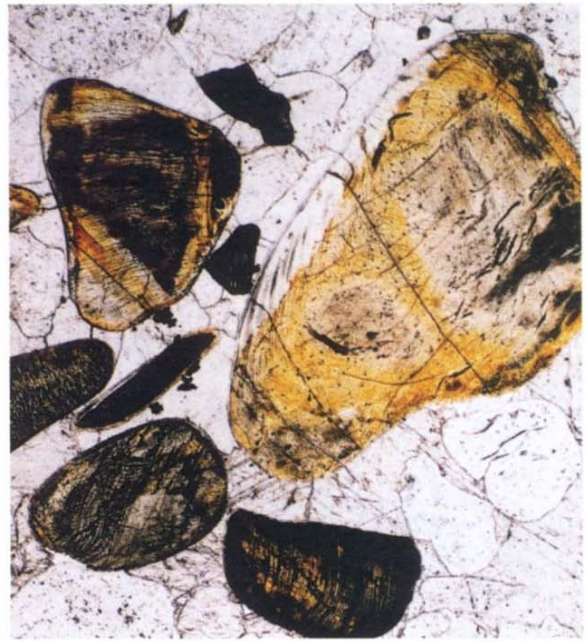

(e)

čtení:

**M.E.Tucker: Sedimentary petrology. 3rd ed. Blackwell, 2001.**
H. Blatt (1992): Sedimentary Petrology. Freeman &Co., New York.
G.S.Odin a A.Matter (1981): De glauconiarum origine. Sedimenntology, 28, 611-641.
C.R.Glenn and 15 others (1994): Phosphorus and phosphorites: Sedimentology and environments of formation. Eclogae Geol. Helv., 87, 3, 747-788.